Integrating faults and past earthquakes into a probabilistic seismic hazard model for peninsular Italy

Alessandro Valentini[1], Francesco Visini[2] and Bruno Pace[1]

[1] DiSPUTer, Università degli Studi "Gabriele d'Annunzio", Chieti, Italy

[2] Istituto Nazionale di Geofisica e Vulcanologia, L'Aquila, Italy

Abstract

Italy is one of the most seismically active countries in Europe. Moderate to strong earthquakes, with magnitudes of up to ~7, have been historically recorded for many active faults. Currently, probabilistic seismic hazard assessments in Italy are mainly based on area source models, in which seismicity is modelled using a number of seismotectonic zones and the occurrence of earthquakes is assumed uniform. However, in the past decade, efforts have increasingly been directed towards using fault sources in seismic hazard models to obtain more detailed and potentially more realistic patterns of ground motion. In our model, we used two categories of earthquake sources. The first involves active faults, and fault slip rates were used to quantify the seismic activity rate. We produced an inventory of all fault sources with details of their geometric, kinematic and energetic properties. The associated parameters were used to compute the total seismic moment rate of each fault. We evaluated the magnitude-frequency distribution (MFD) of each fault source using two models: a characteristic Gaussian model centred ~~on~~ the maximum magnitude and a Truncated Gutenberg-Richter model. The second earthquake source category involves distributed seismicity, ~~and~~ a fixed-radius smoothed approach and a historical catalogue were used to evaluate seismic activity. Under the assumption that deformation is concentrated along faults, we combined the MFD derived from the geometry and slip rates of active faults with the MFD from the spatially smoothed earthquake sources and assumed that the smoothed seismic activity in the vicinity of an active fault gradually decreases by a fault size-driven factor. Additionally, we computed horizontal peak ground acceleration maps for return periods of 475 and 2,475 yrs. Although the ranges and gross spatial distributions of the expected accelerations obtained here are comparable to those obtained through methods involving seismic catalogues and classical zonation models, the spatial pattern of the hazard maps obtained with our model is far more detailed. Our model is characterized by areas that are more hazardous and that correspond to mapped active faults, while previous models yield expected accelerations that are almost uniformly distributed across large regions. In addition, we conducted sensitivity tests to

determine the impact on the hazard results of the earthquake rates derived from two MFD models for faults and to determine the relative contributions of faults versus distributed seismic activity. We believe that our model represents advancements in terms of the input data (quantity and quality) and methodology used in the field of fault-based regional seismic hazard modelling in Italy.

1. Introduction

In this paper, we present the results of ~~a new probabilistic seismic hazard (PSH) model~~ for Italy that includes significant advances in the use of integrated active fault and seismological data. The use of active faults as an input for ~~PSH~~ analysis is a consolidated approach in many countries characterized by high strain rates and seismic releases, as shown, for example, by Field et al. (2015) in California and Stirling et al. (2012) in New Zealand. ~~However~~, in recent years, active fault data have also been successfully integrated into ~~PSH assessments~~ in regions with moderate-to-low strain rates, such as SE Spain (e.g., Garcia-Mayordomo et al., 2007), France (e.g., Scotti et al., 2014), and central Italy (e.g., Peruzza et al., 2011).

In Europe, a working group of the European Seismological Commission, named *Fault2SHA*, is discussing fault-based seismic hazard modelling (https://sites.google.com/site/linkingfaultpsha/home). The working group, born to motivate exchanges between field geologists, fault modellers and seismic hazard practitioners, organizes workshops, conference sessions, and special issues and stimulates collaborations between researchers. The work we are presenting here stems from the activities of the *Fault2SHA* working group.

Combining active faults and background sources is one of the main issues in this type of approach. Although the methodology remains far from identifying a standard procedure, common approaches combine active faults and background sources by applying a threshold magnitude, generally between 5.5 and 7, above which seismicity is modelled as occurring on faults and below which seismicity is modelled via a smoothed approach (e.g., Akinci et al., 2009), area sources (e.g., the so-called FSBG model in ~~SHARE;~~ Woessner et al., 2015) or a combination of the two (Field et al., 2015; Pace et al., 2006).

Another important issue in the use of active faults in ~~PSHA is assigning the "correct" magnitude-frequency distribution (MFD) to the fault sources.~~ Gutenberg-Richter (GR)

and characteristic earthquake models are commonly used, and the choice sometimes depends on the knowledge of the fault and data availability. Often, the choice of the "appropriate" MFD for each fault source is a difficult task because palaeoseismological studies are scarce, and it is often difficult to establish clear relationships between mapped faults and historical seismicity. Recently, Field et al. (2017) discussed the effects and complexity of the choice, highlighting how often the GR model results are not consistent with data; however, in other cases, uncharacteristic behaviour, with rates smaller than the maximum, are possible. The discussion is open (see for example the discussion by Kagan et al., 2012) and far from being solved with the available observations, including both seismological and/or geological/paleoseismological observations. In this work, we explore the calculations of these two MFDs, a characteristic Gaussian model and a Truncated Gutenberg-Richter model, to explore the epistemic uncertainties and to consider a *Mixed model* as a so-called "expert judgement" model. This approach is useful for comparative analysis, and which we assigned one of the two MFDs to each fault source. The rationale of the choice of the MFD of each fault source is explained in detail later in this paper. However, this approach obviously does not solve the issue, and the choice of MFD remains an open question in fault-based PSHA.

In Italy, the current national PSH model for building code (Stucchi et al., 2011) is based on area sources and the classical Cornell approach (Cornell, 1968), in which the occurrence of earthquakes is assumed uniform in the defined seismotectonic zones. However, we believe that more efforts must be directed towards using geological data (e.g., fault sources and paleoseismological information) in ~~PSH models~~ to obtain detailed patterns of ground motion, extend the observational time required to capture the recurrence of large-magnitude events and improve the reliability of seismic hazard assessments. In fact, as highlighted by the 2016-2017 seismic sequences in central Italy, a zone-based ~~PSH~~ is not able to model local spatial variations in ground motion (Meletti et al., 2016), whereas a fault-based model can provide insights for aftershock time-dependent ~~PSH~~ analysis (Peruzza et al., 2016). In conclusion, even if the main purpose of this work is to integrate active faults into hazard calculations for the Italian territory, this study does not represent an official update of the seismic hazard model of Italy.

2. Source Inputs

Two earthquake-source inputs are considered in this work. The first is a ~~fault source input that is based on~~ active faults and uses the geometries and slip rates of known active faults to compute activity rates over a certain range of magnitude. The second is a classical smoothed approach that accounts for the rates of expected earthquakes with a minimum moment magnitude (Mw) of 4.5 but excludes earthquakes associated with known faults based on a modified earthquake catalogue. Note that our ~~PSH~~ model requires the combination of the two source inputs related to the locations of expected seismicity rates into a ~~single model~~. Therefore, these two earthquake-source inputs are not independent but complementary, in both the magnitude and frequency distribution, and together account for ~~all~~ seismicity in Italy.

In the following subsections, we describe the two source inputs and how they are combined in the ~~PSH~~ model.

2.1 Fault Source Input

In seismic hazard assessment, an active fault is a structure that exhibits evidence of activity in the late Quaternary (i.e., in the past 125 kyr), has a demonstrable or potential capability of generating major earthquakes and is capable of future reactivation (see Machette, 2000 for a discussion on terminology). The evidence of Quaternary activity can be geomorphological and/or paleoseismological when activation information from instrumental seismic sequences and/or association to historical earthquakes is not available. Fault source ~~inputs~~ are useful for seismic hazard studies, and we compiled a database for Italy via the analysis and synthesis of neotectonic and seismotectonic data from approximately 90 published studies of 110 faults across Italy. Our database included, but was not limited to, the Database of Individual Seismogenic Sources (DISS vers. 3.2.0, http://diss.rm.ingv.it/diss/), which is already available for Italy. It is important to highlight that the DISS is currently composed of two main categories of seismogenic sources: individual and composite sources. The latter are defined by the DISS' authors as "*simplified and three-dimensional representation of a crustal fault containing an unspecified number of seismogenic sources that cannot be singled out. Composite seismogenic sources are not associated with a specific set of earthquakes or earthquake distribution*", and

therefore are not useful for our PSHA approach; the former is "*a simplified and three-dimensional representation of a rectangular fault plane. Individual seismogenic sources are assumed to exhibit characteristic behaviour with respect to rupture length/width and expected magnitude*" (http://diss.rm.ingv.it/diss/index.php/about/13-introduction). Even if in agreement with our approach, we note that some of the individual seismogenic sources in the DISS are based on geological and paleoseismological information, and many others used the *Boxer* code (Gasperini et al., 1999) to calculate the epicentre, moment magnitude, size and orientation of a seismic source from observed macroseismic intensities. We carefully analysed the individual sources and some related issues: (i) the lack of updating of the geological information of some individual sources and (ii) the nonconformity between the input data used by DISS in *Boxer* and the latest historical seismicity (CPTI15) and macroseismic intensity (DBMI15) publications. Thus, we performed a full review of the fault database. We then compiled a fault source database as a synthesis of works published over the past twenty years, including DISS, using all updated and available geological, paleoseismological and seismological data (see the supplemental files for a complete list of references). We consider our database as complete as possible in terms of individual seismogenic sources, and it contains all the parameters necessary to construct an input dataset for fault-based PSHA.

The resulting database of normal and strike-slip active and seismogenic faults in peninsular Italy (Fig. 1, Tables 1 and 2; see the supplemental files) includes all the available geometric, kinematic, slip rate and earthquake source-related information. In the case of missing data regarding the geometric parameters of dip and rake, we assumed typical dip and rake values of 60° and -90°, respectively, for normal faults and 90° and 0° or 180°, respectively, for strike-slip faults. In this paper, only normal and strike-slip faults are used as fault source inputs. We decided not to include thrust faults in the present study because, with the methodology proposed in this study (as discussed later in the text), the maximum size of a single-rupture segment must be defined, and segmentation criteria have not been established for large thrust zones. Moreover, our method uses ~~slip rates~~ to derive active seismicity rates, and sufficient knowledge of these values is not available for thrust faults in Italy. Because some areas of Italy, such as the NW sector of the Alps, Po Valley, the offshore sector of the central Adriatic Sea, and SW Sicily, may be excluded by this limitation, we are

considering an update to our approach to include thrust faults and volcanic sources in a future study. The upper and lower boundaries of the seismogenic layer are mainly derived from the analysis of Stucchi et al. (2011) of the Italian national seismic hazard model and locally refined by more detailed studies (Boncio et al., 2011; Peruzza et al., 2011; Ferranti et al., 2014).

Based on the compiled database, we explored three main ~~issues~~ associated with defining a fault source input: the slip rate evaluation, the segmentation model and the expected seismicity rate calculation.

2.1.1 Slip rates

Slip rates control fault-based seismic hazards (Main, 1996, Roberts et al., 2004; Bull et al., 2006; Visini and Pace, 2014) and reflect the velocities of the mechanisms that operate during continental deformation (e.g., Cowie et al., 2005). Moreover, long-term observations of faults in various tectonic contexts have shown that slip rates vary in space and time (e.g., Bull et al., 2006; Nicol et al., 2006, 2010, McClymont et al., 2009; Gunderson et al., 2013; Benedetti et al., 2013, D'Amato et al., 2016), and numerical simulations (e.g., Robinson et al., 2009; Cowie et al., 2012; Visini and Pace, 2014) suggest that variability mainly occurs in response to interactions between adjacent faults. Therefore, understanding the temporal variability in fault slip rates is a key point in understanding the earthquake recurrence rates and their variability.

In this work, we used the mean of the minimum and maximum slip rate values listed in Table 1 and assumed that it is representative of the long-term behaviour (over the past 15 ky in the Apennines). These values were derived from approximately 65 available neotectonics, palaeoseismology and seismotectonics papers (see the supplemental files). To evaluate the long-term slip rate, which is representative of the average slip behaviour, and its variability over time, we used slip rates determined in different ways and at different time scales (e.g., at the decadal scale based on geodetic data or at longer scales based on the displacement of Holocene or Plio-Pleistocene horizons). Because a direct comparison of slip rates over different time intervals obtained by different methods may be misleading (Nicol et al., 2009), we cannot exclude the possibility that epistemic uncertainties could affect the original

data in some cases. The discussion of these possible biases and their evaluation via statistically derived approaches (e.g., Gardner et al., 1987; Finnegan et al., 2014; Gallen et al., 2015) is beyond the scope of this paper and will be explored in future work. Moreover, we are assuming that slip rate values used are representative of seismic movements, and aseismic factors are not taken into account. Therefore, we believe that investigating the effect of this assumption could be another issue explored in future work; for example, by differentiating between aseismic slip factors in different tectonic contexts.

Because 28 faults had no measured slip (or throw) rate (Fig. 1a), we proposed a statistically derived approach to assign a slip rate to these faults. Based on the slip rate spatial distribution shown in Figure 1b, we subdivided the fault database into three large regions–the Northern Apennines, Central-Southern Apennines and Calabria-Sicilian coast–and analysed the slip rate distribution in these three areas. In Figure 1b, the slip rates tend to increase from north to south. The fault slip rates in the Northern Apennines range from 0.3 to 0.8 mm/yr, with the most common ranging from approximately 0.5-0.6 mm/yr; the slip rates in the Central-Southern Apennines range from 0.3 to 1.0, and the most common rate is approximately 0.3 mm/yr; and the slip rates in the southern area (Calabria and Sicily) range from 0.9 to 1.8, with the most common being approximately 0.9 mm/yr.

The first step in assigning an average slip rate and a range of variability to the faults with unknown values is to identify the most representative distribution among known probability density functions using the slip rate data from each of the three areas. We test five well-known probability density functions (*Weibull*, *normal*, *exponential*, *Inverse Gaussian* and *gamma*) against mean slip rate observations. The resulting function with the highest log-likelihood is the *normal* function in all three areas. Thus, the mean value of the *normal* distribution is assigned to the faults with unknown values. We assign a value of 0.58 mm/yr to faults in the northern area, 0.64 mm/yr to faults in the Central-Southern area, and 1.10 mm/yr to faults in the Calabria-Sicilian area. To assign a range of slip rate variability to each of the three areas, we test the same probability density functions against slip rate variability observations. Similar to the mean slip rate, the probability density function with the highest log-likelihood is the *normal* function in all three areas. We assign a value of 0.25 mm/yr to the faults

in the northern area, 0.29 mm/yr to the faults in the Central-Southern area, and 0.35 mm/yr to the faults in the Calabria-Sicilian area.

2.1.2 Segmentation rules for delineating fault sources

An important issue in the definition of a fault source input is the formulation of segmentation rules. In fact, the question of whether structural segment boundaries along multisegment active faults act as persistent barriers to a single rupture is critical to defining the maximum seismogenic potential of fault sources. In our case, the rationale behind the definition of a fault source is based on the assumption that the geometric and kinematic features of a fault source are expressions of its seismogenic potential and that its dimensions are compatible for hosting major (Mw ≥ 5.5) earthquakes. Therefore, a fault source is considered a fault or an ensemble of faults that slip together during an individual major earthquake. A fault source is defined by a *seismogenic master fault* and its surface projection (Fig. 2a). *Seismogenic master faults* are separated from each other by first-order structural or geometrical complexities. Following the suggestions by Boncio et al. (2004) and Field et al. (2015), we imposed the following segmentation rules in our case study: (i) 4-km fault gaps among aligned structures; (ii) intersections with cross structures (often transfer faults) extending 4 km along strike and oriented at nearly right angles to the intersecting faults; (iii) overlapping or underlapping en echelon arrangements with separations between faults of 4 km; (iv) bending ≥ 60° for more than 4 km; (v) average slip rate variability along a strike greater than or equal to 50%; and (vi) changes in seismogenic thickness greater than 5 km among aligned structures. Example applications of the above rules are illustrated in Figure 2a.

By applying the above rules to our fault database, the 110 faults yielded 86 fault sources: 9 strike-slip sources and 77 normal-slip sources. The longest fault source is *Castelluccio dei Sauri* (fault number (*id in Table 1)* 42, L = 93.2 km), and the shortest is *Castrovillari* (*id* 63, L = 10.3 km). The mean length is 30 km. The dip angle varies from 30° to 90°, and 70% of the fault sources have dip angles between 50° and 60°. The mean value of seismogenic thickness (ST) is approximately 12 km. The source with the largest ST is *Mattinata* (*id* 41, ST = 25 km), and the source with the thinnest

ST is *Monte Santa Maria Tiberina* (*id* 9, ST = 2.5 km) due to the presence of an east-dipping low angle normal fault, the Alto-Tiberina Fault (Boncio et al., 2000), located a few kilometres west of the Monte Santa Maria Tiberina fault. Observed values of maximum magnitude (M_w) have been assigned to 35 fault sources (based on Table 2), and the values vary from 5.90 to 7.32. The fault source inputs are shown in Figure 3.

2.1.3 Expected seismicity rates

Each fault source is characterized by data, such as kinematic, geometry and slip rate information, that we use as inputs for the FiSH code (Pace et al., 2016) to calculate the global budget of the seismic moment rate allowed by the structure. This calculation is based on predefined size-magnitude relationships in terms of the maximum magnitude (M_{max}) and the associated mean recurrence time (T_{mean}). Table 1 summarizes the geometric parameters used as FiSH input parameters for each fault source (seismogenic box) shown in Figure 3. To evaluate M_{max} of each source, according to Pace et al., (2016) we first computed and then combined up to five M_{max} values (see the example of the Paganica fault source in Fig. 2b, details in Pace et al., 2016). Specifically, these five M_{max} values are as follows: *MM0* based on the calculated scalar seismic moment (M_0) and the application of the standard formula $M_w = 2/3\ (logM_0 - 9.1)$ (Hanks and Kanamori, 1979; IASPEI, 2005); two magnitude values using the Wells and Coppersmith (1994) empirical relationships for the maximum subsurface rupture length (MRLD) and maximum rupture area (MRA); a value that corresponds to the maximum observed magnitude (MObs), if available; and a value (MASP, ASP for aspect ratio) computed by reducing the fault length input if the aspect ratio (W/L) is smaller than the value evaluated by the relation between the aspect ratio and rupture length of observed earthquake ruptures, as derived by Peruzza and Pace (2002) (not in the case of Paganica in Fig. 2b). Although incorrect to consider MObs a possible M_{max} value and treat it the same as other estimations, in some cases, it was useful to constrain the seismogenic potentials of individual seismogenic sources. As an example, for the *Irpinia Fault* (id 51 in Tables 1 and 2), the characteristics of the 1980 earthquake (Mw~6.9) can be used to evaluate M_{max} via comparison with the M_{max} derived from scaling relationships. In such cases, we (i) calculated the maximum expected magnitude

(M_{max1}) and the relative uncertainties using only the scaling relationships and (ii) compared the maximum of observed magnitudes of the earthquakes potentially associated with the fault. If MObs was within the range of M_{max} ± 1 standard deviation, we considered the value and recalculated a new M_{max} (M_{max2}) with a new uncertainty. If MObs was larger than M_{max1}, we reviewed the fault geometry and/or the earthquake-source association.

Because all the empirical relationships, as well as observed historical and recent magnitudes of earthquakes, are affected by uncertainties, the *MomentBalance* (MB) ~~portion~~ of the FiSH code (Pace et al., 2016) was used to account for these uncertainties. MB computes a ~~probability density function~~ for each magnitude derived from empirical relationships or observations and summarizes the results as a maximum magnitude value with a standard deviation. The uncertainties in the empirical scaling relationship are taken from the studies of Wells and Coppersmith (1994), Peruzza and Pace (2002) and Leonard (2010). Currently, the uncertainty in magnitude associated with the seismic moment is fixed and set to 0.3, whereas the catalogue defines the uncertainty in MObs. Moreover, to combine the evaluated maximum magnitudes, MB creates a probability curve for each magnitude by assuming a normal distribution (Fig. 2). We assumed an untruncated normal distribution of magnitudes at both sides. MB successively sums the probability density curves and fits the summed curve to a normal distribution to obtain the mean of the maximum magnitude M_{max} and its standard deviation.

Thus, a unique M_{max} with a standard deviation is computed for each source, and this value represents the maximum rupture that is allowed by the fault geometry and the rheological properties.

Finally, to obtain the mean recurrence time of M_{max} (i.e., T_{mean}), we use the criterion of "segment seismic moment conservation" proposed by Field et al. (1999). This criterion divides the seismic moment that corresponds to M_{max} by the moment rate for given a slip rate:

$$T_{mean} = \frac{1}{Char\_Rate} = \frac{10^{1.5\,Mmax^{9.1}}}{\mu VLW} \quad (1)$$

where T_{mean} is the mean recurrence time in years, Char_Rate is the annual mean rate of occurrence, M_{max} is the computed mean maximum magnitude, μ is the shear modulus, V is the average long-term slip rate, and L and W are geometrical parameters of the fault along-strike rupture length and downdip width, respectively. This approach was used for both MFDs in this study, and, in particular, we evaluated M_{max} and T_{mean} based on the fault geometry and the slip rate of each individual source. Additionally, we calculated the total expected seismic moment rate using equation 1. Then, we partitioned the total expected seismic moment rate based on a range given by M_{max} ± 1 standard deviation following a Gaussian distribution.

After the fault source is entered as input, the seismic moment rate is calculated, M_{max} (Fig. 2b) and T_{mean} are defined for each source, we computed the MFDs of expected seismicity. For each fault source, we use two "end-member" MFD models: (i) a *Characteristic Gaussian* (*CHG*) model, a symmetric Gaussian curve (applied to the incremental MFD values) centred on the M_{max} value of each fault with a range of magnitudes equal to 1-sigma, and (ii) a *Truncated Gutenberg-Richter* (*TGR, Ordaz, 1999; Kagan, 2002*) model, with M_{max} as the upper threshold and M_w = 5.5 as the minimum threshold for all sources. The b-values are constant and equal to 1.0 for all faults, and they are obtained by the interpolation of earthquake data from the CPTI15 catalogue, as single-source events are insufficient for calculating the required statistics. The a-values were computed with the ActivityRate tool of the FiSH code. ActivityRate balances the total expected seismic moment rate with the seismic moment rate that was obtained based on M_{max} and T_{mean} (details in Pace et al., 2016). In Figure 2c, we show an example of the expected seismicity rates in terms of the annual cumulative rates for the Paganica source using the two above-described MFDs.

Finally, we create a so-called "expert judgement" model, called the *Mixed* model, to determine the MFD for each fault source based on the earthquake-source associations. In this case, we decided that if an earthquake assigned to a fault source (see Table 2 for earthquake-source associations) has a magnitude lower than the magnitude range in the curve of the *CHG* model distribution, the *TGR* model is applied to that fault source. Otherwise, the *CHG* model, which peaks at the calculated M_{max}, is applied. Of course, errors in this approach can originate from the misallocation of historical earthquakes, and we cannot exclude the possibility that potentially active faults responsible for historical earthquakes have not yet been

mapped. The MFD model assigned to each fault source in our *Mixed* model is shown in Figure 3.

2.2 Distributed Source Inputs

Introducing distributed earthquakes into the ~~PSH~~ model is necessary because researchers have not been able to identify a causative source (i.e., a mapped fault) for important earthquakes in the historical catalogue. This lack of correlation between earthquakes and faults may be related to (i) interseismic strain accumulation in areas between major faults, (ii) earthquakes occurring on unknown or blind faults, (iii) earthquakes occurring on unmapped faults characterized by slip rates lower than the rates of erosional processes, and/or (iv) the general lack of surface ruptures associated with faults generating $M_w < 5.5$ earthquakes.

We used the historical catalogue of earthquakes (CPTI15; Rovida et al., 2016; Fig. 4) to model the occurrence of moderate-to-large (Mw ≥ 4.5) earthquakes. The catalogue consists of 4,427 events and covers approximately the last one thousand years from 01/01/1005 to 28/12/2014. Before using the catalogue, we removed all events not considered mainshocks via a declustering filter (Gardner and Knopoff, 1977). This process resulted in a complete catalogue composed of 1,839 independent events. Moreover, to avoid any artificial effects related to double counting due to the use of two seismicity sources, i.e., the fault sources and the distributed seismicity sources, we removed events associated with known active faults from the CPTI15 earthquake catalogue. If the causative fault of an earthquake is known, that earthquake does not need to be included in the seismicity smoothing procedure. The earthquake-source association is based on neotectonics, palaeoseismology and seismotectonics papers (see the supplemental files) and, in a few cases, macroseismic intensity maps. In Table 2, we listed the earthquakes with known causative fault sources. The differences in the smoothed rates given by eq. (2) using the complete and modified catalogues are shown in Figure 5.

We applied the standard methodology developed by Frankel (1995) to estimate the density of seismicity in a grid with latitudinal and longitudinal spacing of 0.05°. The smoothed rate of events in each cell *i* is determined as follows:

$$n_i = \frac{\Sigma_j n_j e^{\frac{-\Delta_{ij}^2}{c^2}}}{\Sigma_j e^{\frac{-\Delta_{ij}^2}{c^2}}} \qquad (2)$$

where n_i is the cumulative rate of earthquakes with magnitudes greater than the completeness magnitude Mc in each cell *i* of the grid and Δ*ij* is the distance between the centres of grid cells *i* and *j*. The parameter *c* is the correlation distance. The sum is calculated in cells *j* within a distance of 3*c* of cell *i*.

To compute earthquake rates, we adopted the completeness magnitude thresholds over different periods given by Stucchi et al. (2011) for five large zones (Fig. 4).

To optimize the smoothing distance Δ in eq. (2), we divided the earthquake catalogue into four 10-yr disjoint learning and target periods from the 1960s to the 1990s. For each pair of learning and target catalogues, we used the probability gain per earthquake to find the optimal smoothing distance (Kagan and Knopoff, 1977; Helmstetter et al., 2007). After assuming a spatially uniform earthquake density model as a reference model, the probability gain per earthquake G of a candidate model relative to a reference model is given by the following equation:

$$G = exp(\frac{L-L_0}{N}) \qquad (3)$$

where N is the number of events in the target catalogue and *L* and L_0 are the joint log-likelihoods of the candidate model and reference model, respectively. Under the assumption of a Poisson earthquake distribution, the joint log-likelihood of a model is given as follows:

$$L = \sum_{i_x=1}^{N_x} \sum_{j_y=1}^{N_y} log\ p\left[\lambda(i_x, i_y), \omega\right] \quad (4)$$

where *p* is the Poisson probability, *λ* is the spatial density, ω is the number of observed events during the target period, and the parameters i_x and i_y denote each corresponding longitude-latitude cell.

Figure 6 shows that for the four different pairs of learning-target catalogues, the optimal smoothing distance *c* ranges from 30-40 km. Finally, the mean of all the

probability gains per earthquake yields a maximum smoothing distance of 30 km (Fig. 6), which is then used in eq. (2).

The b-value of the GR distribution is calculated on a regional basis using the maximum-likelihood method of Weichert (1980), which allows multiple periods with varying completeness levels to be combined. Following the approach recently proposed by Kamer and Hiemer (2015), we used a penalized likelihood-based method for the spatial estimation of the GR b-values based on the Voronoi tessellation of space without tectonic dependency. The whole Italian territory has been divided into a grid with a longitude/latitude spacing of 0.05°, and the centres of the grid cells represent the possible centres of Voronoi polygons. We vary the number of Voronoi polygons, Nv, from 3 to 50, generating 1000 tessellations for each Nv. The summed log-likelihood of each obtained tessellation is compared with the log-likelihood given by the simplest model (prior model) obtained using the entire earthquake dataset. We find that 673 random realizations led to better performance than the prior model. Thus, we calculate an ensemble model using these 673 solutions, and the mean b-value of each grid node is shown in Figure 4.

The maximum magnitude M_{max} assigned to each node of the grid, the nodal planes and the depths have been taken from the SHARE European project (Woessner et al., 2015). The SHARE project evaluated the maximum magnitudes of large areas of Europe based on a joint procedure involving historical observations and tectonic regionalization. We adopted the lowest of the maximum magnitudes proposed by SHARE, but evaluating the impact of different maximum magnitudes is beyond the scope of this work.

Finally, the rates of expected seismicity for each node of the grid are assumed to follow the TGR model (Kagan 2002):

$$\lambda(M) = \lambda_0 \frac{\exp(-\beta M) - \exp(-\beta M_u)}{\exp(-\beta M_0) - \exp(-\beta M_u)} \qquad (5)$$

where the magnitude (M) is in the range of M_0 (minimum magnitude) to M_u (upper or maximum magnitude); otherwise $\lambda(M)$ is 0. Additionally, λ_0 is the smoothed rate of earthquakes at $M_w = 4.5$ and $\beta = b \ln(10)$.

2.3 Combining Fault and Distributed Sources

To combine the two source inputs, we introduced a distance-dependent linear weighting function, such that the contribution from the distributed sources linearly decreases from 1 to 0 with decreasing distance from the fault. The expected seismicity rates of the distributed sources start at Mw = 4.5, which is lower than the minimum magnitude of the fault sources, and the weighting function is only applicable in the magnitude range overlapping the MFD of each fault. This weighting function is based on the assumption that faults tend to modify the surrounding deformation field (Fig. 7), and this assumption is explained in detail later in this paper.

During fault system evolution, the increase in the size of a fault through linking with other faults results in an increase in displacement that is proportional to the quantity of strain accommodated by the fault (Kostrov, 1974). Under a constant regional strain rate, the activity of arranged across strike must eventually decrease (Nicol et al., 1997; Cowie, 1998; Roberts et al., 2004). Using an analogue modelling, Mansfield and Cartwrigth (2001) showed that faults grow via cycles of overlap, relay formation, breaching and linkage between neighbouring segments across a wide range of scales. During the evolution of a system, the merging of neighbour faults, mostly along the strike, results in the formation of major faults, which are associated with the majority of displacement. These major faults are surrounded by minor faults, which are associated with lower degrees of displacement. To highlight the spatial patterns of major and minor faults, Figures 7a and 7b present diagrams from the Mansfield and Cartwright (2001) experiment in two different stages: the approximate midpoint of the sequence and the end of the sequence. Numerical modelling performed by Cowie et al. (1993) yielded similar evolutionary features for major and minor faults. The numerical fault simulation of Cowie et al. (1993) was able to reproduce the development of a normal fault system from the early nucleation stage, including interactions with adjacent faults, to full linkage and the formation of a large through fault. The model also captures the increase in the displacement rate of a large linked fault. In Figures 7c and 7d, we focus on two stages of the simulation (from Cowie et al., 1993): the stage in which the fault segments have formed and some have become linked and the final stage of the simulation.

Notably, the spatial distributions of major and minor faults are very similar in the experiments of both Mansfield and Cartwrigth (2001) and Cowie et al. (1993), as shown in Figures 7a-d. Developments during the early stage of major fault formation appear to control the location and evolution of future faults, with some areas where no major faults develop. The long-term evolution of a fault system is the consequence of the progressive cumulative effects of the slip history, i.e., earthquake occurrence, of each fault. Large earthquakes are generally thought to produce static and dynamic stress changes in the surrounding areas (King et al., 1994; Stein, 1999; Pace et al., 2014; Verdecchia and Carena, 2016). Static stress changes produce areas of negative stress, also known as shadow zones, and positive stress zones. The spatial distributions of decreases (unloading) and increases (loading) in stress during the long-term slip history of faults likely influence the distance across strike between major faults. Thus, given a known major active fault geometrically capable of hosting a Mw ≥ 5.5 earthquake, the possibility that a future Mw ≥ 5.5 earthquake will occur in the vicinity of the fault, but is not caused by that fault, should decrease as the distance from the fault decreases. Conversely, earthquakes with magnitudes lower than 5.5 and those due to slip along minor faults are likely to occur everywhere within a fault system, including in proximity to a major fault.

In Figure 7e, we illustrate the results of the analogue and numerical modelling of fault system evolution and indicate the areas around major faults where it is unlikely that other major faults develop. In Figure 7f, we show the next step in moving from geologic and structural considerations. In this step, we combine fault sources and distributed seismicity source inputs, which serve as inputs ~~for the PSH model~~. Fault sources are used to model major faults and are represented by a master fault (i.e., one or more major faults) and its projection at the surface. Distributed seismicity is used to model seismicity associated with minor, unknown or unmapped faults. Depending on the positions of distributed seismicity points with respect to the buffer zones around major faults, the rates of expected distributed seismicity remain unmodified or decrease and can even reach zero.

Specifically, we introduced a slip rate and a distance-weighted linear function based on the above reasoning. The probability of the occurrence of an earthquake (Pe) with a Mw greater than or equal to the minimum magnitude of the fault is as follows:

$$Pe = \begin{cases} 0, & d \leq 1\ km \\ d/d_{max}, & 1\ km < d \leq d_{max} \\ 1, & d > d_{max} \end{cases} \quad (6)$$

where *d* is the Joyner-Boore distance from a fault source. The maximum value of *d* (d_{max}) is controlled by the slip rate of the fault. For faults with slip rates ≥ 1 mm/yr, we assume d_{max} = L/2 (L is the length along the strike, Fig. 2a); for faults with slip rates of 0.3 - 1 mm/yr, d_{max} = L/3; and for faults with slip rates of ≤ 0.3 mm/yr, d_{max} = L/4. The rationale for varying d_{max} is given by a simple assumption: the higher the slip rate is, the larger the deformation field and the higher the value of d_{max}. We applied eq. (6) to the smoothed occurrence rates of the distributed seismogenic sources. Because we consider two fault source inputs, one using only TGR MFD and the other only CHR MFD, and because the MFDs of distributed seismicity grid points in the vicinity of faults are modified with respect to the MFDs of these faults, we obtain two different inputs of distributed seismicity. These two distributed seismogenic source inputs differ because the minimum magnitude of the faults is Mw 5.5 in the TGR model, but this value depends on each fault source dimension in the CHG model, as shown in Figure 8.

Our approach allows incompleteness in the fault database to be bypassed, which is advantageous because all fault databases should be considered incomplete. In our approach, the seismicity is modified only in the vicinity of mapped faults. The remaining areas are fully described by the *distributed* input. With this approach, we do not define areas with reliable fault information, and the locations of currently unknown faults can be easily included when they are discovered in the future.

3. Results and Discussion

To ~~obtain PSH maps~~, we assign the calculated seismicity rates, based on the Poisson hypothesis, to their pertinent geometries, i.e., individual 3D seismogenic sources for the *fault input* and point sources for the *distributed input* (Fig. 8). All the computations are performed using the OpenQuake Engine (~~Global Earthquake Model, 2018~~) with a grid spacing of 0.05° in both latitude and longitude. We used this software because it is open source software developed recently by GEM with the purpose of providing seismic hazard and risk assessments. Moreover, it is widely recognized within the scientific community for its potential. The ground motion

prediction equations (GMPE) of Akkar et al. (2013), Chiou et al., (2008), Faccioli et al., (2010) and Zhao et al., (2006) are used, ~~as suggested by the SHARE European project~~ (Woessner et al., 2015). In addition, we used the GMPE proposed by Bindi et al. (2014) and calibrated using Italian data. We combined all GMPEs into a logic tree with the same weight of 0.2 for each branch. The distance used for each GMPE was the Joyner and Boore distance for Akkar et al. (2013), Bindi et al. (2014) and Chiou et al. (2008) and the closest rupture distance for Faccioli et al. (2010) and Zhao et al. (2006).

The results of the fault source inputs, distributed source inputs, and aggregated model are expressed in terms of peak ground acceleration (PGA) based on exceedance probabilities of 10% and 2% over 50 years, corresponding to return periods of 475 and 2,475 years, respectively (Fig. 9).

To explore the epistemic uncertainty associated with the distribution of activity rates over the range of magnitudes of fault source inputs, we compared the seismic hazard levels obtained based on the TGR and CHG fault source inputs (left column in Fig. 9) using the TGR and CHG MFDs for all the fault sources (details in section 2.1.3). Although both models have the same seismic moment release, the different MFDs generate clear differences. In fact, in the *TGR* model, all faults contribute significantly to the seismic hazard level, whereas in the *CHG* model, only a few faults located in the central Apennines and Calabria contribute to the seismic hazard level. This difference is due to the different shapes of the MFDs in the two models (Fig. 2c). As shown in Figure 8, the percentage of earthquakes with magnitudes between 5.5 and approximately 6, which are likely the main contributors to these levels of seismic hazards, is generally higher in the *TGR* model than in the *CHG* model. At a 2% probability of exceedance in 50 years, all fault sources in the CHG contribute to the seismic hazard level, but the absolute values are still generally higher in the *TGR* model.

The *distributed input* (middle column in Fig. 9) depicts a more uniform shape of the seismic hazard level than that of fault source inputs. A low PGA value of 0.125 g at a 10% probability of exceedance over 50 years and a low value of 0.225 g at a 2% probability of exceedance over 50 years encompass a large part of peninsular Italy

565 and Sicily. Two areas with high seismic hazard levels are located in the central
566 Apennines and northeastern Sicily.

567 The overall model, which was created by combining the fault and distributed source
568 inputs, is shown in the right column of Figure 9. Areas with comparatively high
569 seismic hazard levels, i.e., hazard levels greater than 0.225 g and greater than 0.45
570 g at 50-yr exceedance probabilities of 10% and 2%, respectively, are located
571 throughout the Apennines, in Calabria and in Sicily. The fault source inputs
572 contribute most to the total seismic hazard levels in the Apennines, Calabria and
573 eastern Sicily, where the highest PGA values are observed.

574 Figure 10 shows the contributions to the total seismic hazard level by the *fault* and
575 *distributed* source inputs at a specific site (L'Aquila, 42.400-13.400). Notably, in
576 Figure 10, *distributed* sources dominate the seismic hazard contribution at
577 exceedance probabilities greater than ~81% over 50 years, but the contribution of
578 *fault* sources cannot be neglected. Conversely, at exceedance probabilities of less
579 than ~10% in 50 years, the total hazard level is mainly associated with *fault* source
580 inputs.

581 Figure 11 presents seismic hazard maps for PGAs at 10% and 2% exceedance
582 probabilities in 50 years for *fault* sources, *distributed* sources and a combination of
583 the two. These data were obtained using the above-described *Mixed* model, in which
584 we selected the most "appropriate" MFD model (TGR or CHG) for each fault (as
585 shown in Figure 3). The results of this model therefore have values between those of
586 the two end-members shown in Figure 9.

587 Figure 12 shows the *CHG*, *TGR* and *Mixed* model hazard curves of three sites
588 (Cesena, L'Aquila and Crotone, Fig. 13c). As previously noted, the results of the
589 *Mixed* model, due to the structure of the model, are between those of the *CHG* and
590 *TGR* models. The relative positions of the hazard curves derived from the two end-
591 member models and the *Mixed* model depend on the number of nearby fault sources
592 that have been modelled using one of the MFD models and on the distance of the
593 site from the faults. For example, in the case of the Crotone site, the majority of the
594 fault sources in the *Mixed* model are modelled using the CHG MFD. Thus, the
595 resulting hazard curve is similar to that of the *CHG* model. For the Cesena site, the

three hazard curves overlap. Because the distance between Cesena and the closest fault sources is approximately 60 km, the impact of the fault input is less than the impact of the *distributed* source input. In this case, the choice of a particular MFD model has a limited impact on the modelling of *distributed* sources. Notably, for an annual frequency of exceedance (*AFOE*) lower than 10^{-4}, the *TGR fault* source input values are generally higher than those of the *CHG* source input, and the three models converge at *AFOE* < 10^{-4}. The resulting seismic hazard estimates depend on the assumed MFD model (*TGR* vs. *CHG*), especially for intermediate-magnitude events (5.5 to ~6.5). Because we assume that the maximum magnitude is imposed by the fault geometry and that the seismic moment release is controlled by the slip rate, the *TGR* model leads to the highest hazard values because this range of magnitude contributes the most to the hazard level.

In Figure 13, we investigated the influences of the Mixed *fault* source inputs and the Mixed *distributed* source inputs on the total hazard level of the entire study area, as well as the variability in the hazard results. The maps in Figure 13a show that the contribution of *fault* inputs to the total hazard level generally decreases as the exceedance probability increases from 2% to 81% in 50 years. At a 2% probability of exceedance in 50 years, the total hazard levels in the Apennines and eastern Sicily are mainly related to faults, whereas at an 81% probability of exceedance in 50 years, the contributions of *fault* inputs are high in local areas of central Italy and southern Calabria.

Moreover, we examined the contributions of *fault* and *distributed* sources along three E-W-oriented profiles in northern, central and southern Italy (Fig. 13b). Note that the contributions are not based on deaggregation but are computed according to the percentage of each source input in the AFOE value of the combined model. In areas with faults, the hazard level estimated by *fault* inputs is generally higher than that estimated by the corresponding *distributed* source inputs. Notable exceptions are present in areas proximal to slow-slipping active faults at an 81% probability of exceedance in 50 years (profile A), such as those at the eastern and western boundaries of the fault area in central Italy (profile B), and in areas where the contribution of the *distributed* source input is equal to that of the *fault* input at a 10% probability of exceedance in 50 years (eastern part of profile C).

The features depicted by the three profiles result from a combination of the slip rates and spatial distributions of faults for *fault* source inputs. This pattern should be considered a critical aspect of using fault models for ~~PSH~~ analysis. In fact, the proposed approach requires a high level of expertise in active tectonics and cautious expert judgement at many levels in the procedure. First, the seismic hazard estimate is based on the definition of a segmentation model, which requires a series of rules based on observations and empirical regression between earthquakes and the size of the causative fault. New data might make it necessary to revise the rules or reconsider the role of the segmentation. In some cases, expert judgement could permit discrimination among different fault source models. Alternatively, all models should be considered branches in a logic tree approach.

Moreover, we propose a fault seismicity input in which the MFD of each fault source has been chosen based on an analysis of the occurrences of earthquakes that can be tentatively or confidently assigned to a certain fault. To describe the fault activity, we applied a probability density function to the magnitude, as commonly performed in the literature: the TGR model, where the maximum magnitude is the upper threshold and M_w = 5.5 is the lower threshold for all faults, and the characteristic maximum magnitude model, which consists of a truncated normal distribution centred on the maximum magnitude. Other MFDs have been proposed to model the earthquake recurrence of a fault. For example, Youngs and Coppersmith (1985) proposed a modification to the truncated exponential model to allow for the increased likelihood of characteristic events. However, we focused only on two models, as we believe that instead of a “blind” or qualitative characterization of the MFD of a fault source, future applications of statistical tests of the compatibility between expected earthquake rates and observed historical seismicity could be used as an objective method of identifying the optimal MFD of expected seismicity.

To focus on the general procedure for spatially integrating faults with sources representing distributed (or off-fault) seismicity, we did not investigate the impact of other smoothing procedures on the distributed sources, and we used fixed kernels with a constant bandwidth (as in the works of Kagan and Jackson, 1994; Frankel et al. 1997; Zechar and Jordan, 2010). The testing of adaptive bandwidths (e.g., Stock

and Smith, 2002; Helmstetter et al., 2006, 2007; Werner et al., 2011) or weighted combinations of both models has been reserved for future studies.

Finally, we compared, as shown in Figure 14, the 2013 European Seismic Hazard Model (ESHM13) developed within the SHARE project, the current Italian national seismic hazard map (MPS04) and the results of our model (Mixed model) using the same GMPEs as used in this study. Specifically, for ESHM13, we compared the results to the fault-based hazard map (FSBG model) that accounts for fault sources and background seismicity. The figure shows how the impact of our fault sources is more evident than in FSBG-ESHM13, and the comparison with MPS04 confirms a similar pattern, but with some significant differences at the regional to local scales.

The strength of our approach lies in the integration of different levels of information regarding the active faults in Italy, but the final result is unavoidably linked to the quality of the relevant data. Our work focused on presenting and applying a new approach for evaluating seismic hazards based on active faults and intentionally avoided the introduction of uncertainties due to the use of different segmentation rules or other slip rate values of faults. Moreover, the impact of ground motion predictive models is important in seismic hazard assessment but beyond the scope of this work. Future steps will be devoted to analysing these uncertainties and evaluating their impacts on seismic hazard estimates.

4. Conclusions

We presented ~~our first national scale PSH model of~~ Italy, which summarizes and integrates the fault-based ~~PSH~~ models developed since the publication of Pace et al. in 2006.

The model proposed in this study combines fault source inputs based on over 110 faults grouped into 86 fault sources and distributed source inputs. For each fault source, the maximum magnitude and its uncertainty were derived by applying scaling relationships, and the rates of seismic activity were derived by applying slip rates to seismic moment evaluations and balancing these seismic moments using two MFD models.

To account for unknown faults, a distributed seismicity input was applied following the well-known Frankel (1995) methodology to calculate seismicity parameters.

The fault sources and ~~distributed~~ sources have been integrated via a new approach based on the idea that deformation in the vicinity of an active fault is concentrated along the fault and that the seismic activity in the surrounding region is reduced. In particular, a distance-dependent linear weighting function has been introduced to allow the contribution of distributed sources (in the magnitude range overlapping the MFD of each fault source) to linearly decrease from 1 to 0 with decreasing distance from a fault. The strength of our approach lies in the ability to integrate different levels of available information for active faults that actually exist in Italy (or elsewhere), but the final result is unavoidably linked to the quality of the relevant data.

The ~~PSH~~ maps produced using our model show a hazard pattern similar to that of the current maps at the national scale, but some significant differences in hazard level are present at the regional to local scales (Figure 13).

Moreover, the impact that using different MFD models to derive seismic activity rates has on the hazard maps was investigated. The PGA values in the hazard maps generated by the *TGR* model are higher than those in the hazard maps generated by the *CHG* model. This difference is because the rates of earthquakes with magnitudes from 5.5 to approximately 6 are generally higher in the *TGR* model than in the *CHG* model. Moreover, the relative contributions of fault source inputs and distributed source inputs have been identified in maps and profiles in three sectors of the study area. These profiles show that the hazard level is generally higher where fault inputs are used, and for high probabilities of exceedance, the contribution of *distributed* inputs equals that of *fault* inputs.

Finally, the *Mixed* model was created by selecting the most appropriate MFD model for each fault. All data, including the locations and parameters of fault sources, are provided in the supplemental files of this paper.

~~This new PSH model~~ is not intended to replace, integrate or assess the current official national seismic hazard model of Italy. While some aspects remain to be implemented in our approach (e.g., the integration of reverse/thrust faults in the database, sensitivity tests for the distance-dependent linear weighting function parameters, sensitivity tests for potential different segmentation models, and fault source inputs that account for fault interactions), the proposed model represents

advancements in terms of input data (quantity and quality) and methodology based on a decade of research in the field of fault-based approaches to regional seismic hazard modelling.

References

Akinci, A., Galadini, F., Pantosti, D., Petersen, M., Malagnini, L., and Perkins, D.: Effect of Time Dependence on Probabilistic Seismic-Hazard Maps and Deaggregation for the Central Apennines, Italy, B Seismol Soc Am, 99, 585-610, 2009.

Akkar, S., Sandikkaya, M.A. , Bommer, J.J.: Empirical Ground-Motion Models for Point and Extended-Source Crustal Earthquake Scenarios in Europe and the Middle East, Bulletin of Earthquake Engineering, ISSN:1570-761X, 2013.

Basili, R., Valensise, G., Vannoli, P., Burrato, P., Fracassi, U., Mariano, S., Tiberti, M. M. and Boschi, E.: The Database of Individual Seismogenic Sources (DISS), version 3: Summarizing 20 years of research on Italy's earthquake geology, Tectonophysics, 453, 20- 43, 2008.

Benedetti, L., Manighetti, I., Gaudemer, Y., Finkel, R., Malavieille, J., Pou, K., Arnold, M., Aumaitre, G., Bourles, D., and Keddadouche, K.: Earthquake synchrony and clustering on Fucino faults (Central Italy) as revealed from in situ Cl-36 exposure dating, J Geophys Res-Sol Ea, 118, 4948-4974, 2013.

Bindi, D., Massa, M., Luzi, L., Ameri, G., Pacor, F., Puglia, R., and Augliera, P.: Pan-European ground-motion prediction equations for the average horizontal component of PGA, PGV, and 5%-damped PSA at spectral periods up to 3.0 s using the RESORCE dataset (vol 12, pg 391, 2014), B Earthq Eng, 12, 431-448, 2014.

758 Boncio, P., Brozzetti, F. and Lavecchia G.: Architecture and seismotectonics of a
759 regional Low-Angle Normal Fault zone in Central Italy. Tectonics, 19 (6),
760 1038-1055, 2000.
761 Boncio, P., Lavecchia, G., and Pace, B.: Defining a model of 3D seismogenic
762 sources for Seismic Hazard Assessment applications: The case of central
763 Apennines (Italy), J Seismol, 8, 407-425, 2004.
764 Boncio, P., Pizzi, A., Cavuoto, G., Mancini, M., Piacentini, T., Miccadei, E., Cavinato,
765 G. P., Piscitelli, S., Giocoli, A., Ferretti, G., De Ferrari, R., Gallipoli, M. R.,
766 Mucciarelli, M., Di Fiore, V., Franceschini, A., Pergalani, F., Naso, G., and
767 Macroarea, W. G.: Geological and geophysical characterisation of the
768 Paganica - San Gregorio area after the April 6, 2009 L'Aquila earthquake (M-
769 w 6.3, central Italy): implications for site response, B Geofis Teor Appl, 52,
770 491-512, 2011.
771 Bull, J. M., Barnes, P. M., Lamarche, G., Sanderson, D. J., Cowie, P. A., Taylor, S.
772 K., and Dix, J. K.: High-resolution record of displacement accumulation on an
773 active normal fault: implications for models of slip accumulation during
774 repeated earthquakes, J Struct Geol, 28, 1146-1166, 2006.
775 Chiou, B. S. J. and Youngs, R. R.: An NGA model for the average horizontal
776 component of peak ground motion and response spectra, Earthq Spectra, 24,
777 173-215, 2008.
778 Cornell, C.A.: Engineering seismic risk analysis, Bull. Seism. Soc. Am., 58,1583-
779 1606, 1968.
780 Cowie, P. A.: A healing-reloading feedback control on the growth rate of seismogenic
781 faults, J Struct Geol, 20, 1075-1087, 1998.
782 Cowie, P. A., Roberts, G. P., Bull, J. M., and Visini, F.: Relationships between fault
783 geometry, slip rate variability and earthquake recurrence in extensional
784 settings, Geophys J Int, 189, 143-160, 2012.
785 Cowie, P. A., Underhill, J. R., Behn, M. D., Lin, J., and Gill, C. E.: Spatio-temporal
786 evolution of strain accumulation derived from multi-scale observations of Late
787 Jurassic rifting in the northern North Sea: A critical test of models for
788 lithospheric extension, Earth Planet Sc Lett, 234, 401-419, 2005.

789 Cowie, P. A., Vanneste, C., and Sornette, D.: Statistical Physics Model for the
790 Spatiotemporal Evolution of Faults, J Geophys Res-Sol Ea, 98, 21809-21821,
791 1993.
792 D'amato, D., Pace, B., Di Nicola, L., Stuart, F.M., Visini, F., Azzaro, R., Branca, S.,
793 and Barfod, D.N.: Holocene slip rate variability along the Pernicana fault
794 system (Mt. Etna, Italy): Evidence from offset lava flows: GSA Bulletin,
795 doi:10.1130/B31510.1, 2016.
796 Faccioli, E., Bianchini, A., and Villani, M.: New ground motion prediction equations
797 for t > 1 s and their influence on seismic hazard assessment, In: Proceedings
798 of the University of Tokyo symposium on long-period ground motion and
799 urban disaster mitigation, 2010.
800 Ferranti, L., Palano, M., Cannavo, F., Mazzella, M. E., Oldow, J. S., Gueguen, E.,
801 Mattia, M., and Monaco, C.: Rates of geodetic deformation across active
802 faults in southern Italy, Tectonophysics, 621, 101-122, 2014.
803 Field, E. H., Biasi, G. P., Bird, P., Dawson, T. E., Felzer, K. R., Jackson, D. D.,
804 Johnson, K. M., Jordan, T. H., Madden, C., Michael, A. J., Milner, K. R., Page,
805 M. T., Parsons, T., Powers, P. M., Shaw, B. E., Thatcher, W. R., Weldon, R.
806 J., and Zeng, Y. H.: Long-Term Time-Dependent Probabilities for the Third
807 Uniform California Earthquake Rupture Forecast (UCERF3), B Seismol Soc
808 Am, 105, 511-543, 2015.
809 Field, E. H., Jackson, D. D., and Dolan, J. F.: A mutually consistent seismic-hazard
810 source model for southern California, B Seismol Soc Am, 89, 559-578, 1999.
811 Finnegan, N. J., Schumer, R., and Finnegan, S.: A signature of transience in bedrock
812 river incision rates over timescales of 10(4)-10(7) years, Nature, 505, 391-+,
813 2014.
814 Frankel, A.: Simulating Strong Motions of Large Earthquakes Using Recordings of
815 Small Earthquakes - the Loma-Prieta Mainshock as a Test-Case, B Seismol
816 Soc Am, 85, 1144-1160, 1995.
817 Frankel, A., Mueller, C., Barnhard, T., Perkins, D., Leyendecker, E. V., Dickman, N.,
818 Hanson, S.. and Hopper, M.: Seismic-hazard maps for California, Nevada,
819 and Western Arizona/Utah', U.S. Geological Survey Open-File Rept. 97-130,
820 1997.

821 Gallen, S. F., Pazzaglia, F. J., Wegmann, K. W., Pederson, J. L., and Gardner, T.
822 W.: The dynamic reference frame of rivers and apparent transience in incision
823 rates, Geology, 43, 623-626, 2015.
824 Garcia-Mayordomo, J., Gaspar-Escribano, J. M., and Benito, B.: Seismic hazard
825 assessment of the Province of Murcia (SE Spain): analysis of source
826 contribution to hazard, J Seismol, 11, 453-471, 2007.
827 Gardner, J. K., Knopoff, L.: Is the sequence of earthquakes in Southern California,
828 with aftershocks removed, Poissonian?'. Bulletin of the Seismological Society
829 of America, 64, 1363-1367, 1974.
830 Gardner, T. W., Jorgensen, D. W., Shuman, C., and Lemieux, C. R.: Geomorphic
831 and Tectonic Process Rates - Effects of Measured Time Interval, Geology, 15,
832 259-261, 1987.
833 Gasperini P., Bernardini F., Valensise G. and Boschi E.: Defining Seismogenic
834 Sources from Historical Earthquake Felt Reports, *Bull. Seism. Soc. Am.,* 89,
835 94-110, 1999.
836 GEM: The OpenQuake-engine User Manual. Global Earthquake Model (GEM)
837 Technical Report, doi: 10.13117/GEM.OPENQUAKE.MAN.ENGINE.1.9/01,
838 189 pages, 2016.
839 Gunderson, K. L., Anastasio, D. J., Pazzaglia, F. J., and Picotti, V.: Fault slip rate
840 variability on 10(4)-10(5)yr timescales for the Salsomaggiore blind thrust fault,
841 Northern Apennines, Italy, Tectonophysics, 608, 356-365, 2013.
842 Hanks, T. C., and Kanamori, H.: A moment magnitude scale, Journal of Geophysics
843 Research, 84, 2348–2350, 1979.
844 Helmstetter, A., Kagan, Y. Y., and Jackson, D. D.: Comparison of short-term and
845 time-independent earthquake forecast models for southern California, B
846 Seismol Soc Am, 96, 90-106, 2006.
847 Helmstetter, A., Kagan, Y. Y., and Jackson, D. D.: High-resolution time-independent
848 grid-based forecast for M <= 5 earthquakes in California, Seismol Res Lett,
849 78, 78-86, 2007.
850 International Association of Seismology and Physics of the Earth's Interior (IASPEI):
851 Summary of Magnitude Working Group recommendations on standard
852 procedures for determining earthquake magnitudes from digital data,
853 http://www.iaspei.org/

commissions/CSOI/summary_of_WG_recommendations_2005.pdf (last accessed December 2015), 2005.

Kagan, Y. Y.: Seismic moment distribution revisited: I. Statistical results, Geophys J Int, 148, 520-541, 2002.

Kagan, Y., and Knopoff, L.: Earthquake risk prediction as a stochastic process, Physics of the Earth and Planetary Interiors, 14, 97–108, 1977.

Kagan, Y. Y. and Jackson, D. D.: Long-Term Probabilistic Forecasting of Earthquakes, J Geophys Res-Sol Ea, 99, 13685-13700, 1994.

Kamer, Y. and Hiemer, S.: Data-driven spatial b value estimation with applications to California seismicity: To b or not to b, J Geophys Res-Sol Ea, 120, 5191-5214, 2015.

King, G. C. P., Stein, R. S., and Lin, J.: Static Stress Changes and the Triggering of Earthquakes, B Seismol Soc Am, 84, 935-953, 1994.

Kostrov, V. V.: Seismic moment and energy of earthquakes, and seismic flow of rock, Physic of the Solid Earth, 1, 23-44, 1974.

Leonard, M.: Earthquake fault scaling: Self-consistent relating of rupture length, width, average displacement, and moment release. Bulletin of the Seismological Society of America, 100(5A), 1971- 1988, 2010.

Machette, M.N.: Active, capable, and potentially active faults; a paleoseismic perspective, J. Geodyn., 29, 387–392, 2000.

Main, I.: Statistical physics, seismogenesis, and seismic hazard, Rev Geophys, 34, 433-462, 1996.

Mansfield, C. and Cartwright, J.: Fault growth by linkage: observations and implications from analogue models, J Struct Geol, 23, 745-763, 2001.

Meletti, C., Visini, F., D'Amico, V., and Rovida A.: Seismic hazard in central Italy and the 2016 Amatrice earthquake, Annals of Geophysics, 59, doi:10.4401/ag-7248, 2016.

McClymont, A. F., Villamor, P., and Green, A. G.: Assessing the contribution of off-fault deformation to slip-rate estimates within the Taupo Rift, New Zealand, using 3-D ground-penetrating radar surveying and trenching, Terra Nova, 21, 446-451, 2009a.

McClymont, A. F., Villamor, P., and Green, A. G.: Fault displacement accumulation and slip rate variability within the Taupo Rift (New Zealand) based on trench and 3-D ground-penetrating radar data, Tectonics, 28, 2009b.

888 Nicol, A., Walsh, J., Berryman, K., and Villamor, P.: Interdependence of fault
889 displacement rates and paleoearthquakes in an active rift, Geology, 34, 865-
890 868, 2006.
891 Nicol, A., Walsh, J., Mouslopoulou, V., and Villamor, P.: Earthquake histories and
892 Holocene acceleration of fault displacement rates, Geology, 37, 911-914,
893 2009.
894 Nicol, A., Walsh, J. J., Villamor, P., Seebeck, H., and Berryman, K. R.: Normal fault
895 interactions, paleoearthquakes and growth in an active rift, J Struct Geol, 32,
896 1101-1113, 2010.
897 Nicol, A., Walsh, J. J., Watterson, J., and Underhill, J. R.: Displacement rates of
898 normal faults, Nature, 390, 157-159, 1997.
899 Ordaz, M. and Reyes, C.: Earthquake hazard in Mexico City: Observations versus
900 computations, B Seismol Soc Am, 89, 1379-1383, 1999.
901 Pace, B., Bocchini, G. M., and Boncio, P.: Do static stress changes of a moderate-
902 magnitude earthquake significantly modify the regional seismic hazard? Hints
903 from the L'Aquila 2009 normal-faulting earthquake (Mw 6.3, central Italy),
904 Terra Nova, 26, 430-439, 2014.
905 Pace, B., Peruzza, L., Lavecchia, G., and Boncio, P.: Layered seismogenic source
906 model and probabilistic seismic-hazard analyses in central Italy, B Seismol
907 Soc Am, 96, 107-132, 2006.
908 Pace, B., Visini, F., and Peruzza, L.: FiSH: MATLAB Tools to Turn Fault Data into
909 Seismic-Hazard Models, Seismol Res Lett, 87, 374-386, 2016.
910 Peruzza, L., and Pace B.: Sensitivity analysis for seismic source characteristics to
911 probabilistic seismic hazard assessment in central Apennines (Abruzzo area),
912 Bollettino di Geofisica Teorica ed Applicata 43, 79–100, 2002.
913 Peruzza, L., Pace, B., and Visini, F.: Fault-Based Earthquake Rupture Forecast in
914 Central Italy: Remarks after the L'Aquila M-w 6.3 Event, B Seismol Soc Am,
915 101, 404-412, 2011.
916 Peruzza, L., Gee, R., Pace, B., Roberts, G., Scotti, O., Visini,F., Benedetti, L., and
917 Pagani, M.: PSHA after a strong earthquake: hints for the recovery, Annals of
918 Geophysics, 59, doi:10.4401/ag-7257, 2016
919 Roberts, G. P., Cowie, P., Papanikolaou, I., and Michetti, A. M.: Fault scaling
920 relationships, deformation rates and seismic hazards: an example from the
921 Lazio-Abruzzo Apennines, central Italy, J Struct Geol, 26, 377-398, 2004.

922 Roberts, G. P. and Michetti, A. M.: Spatial and temporal variations in growth rates
923 along active normal fault systems: an example from The Lazio-Abruzzo
924 Apennines, central Italy, J Struct Geol, 26, 339-376, 2004.
925 Robinson, R., Nicol, A., Walsh, J. J., and Villamor, P.: Features of earthquake
926 occurrence in a complex normal fault network: Results from a synthetic
927 seismicity model of the Taupo Rift, New Zealand, J Geophys Res-Sol Ea, 114,
928 2009.
929 Rovida, A., Locati, M., Camassi, R., Lolli, B., and Gasperini P.: CPTI15, the 2015
930 version of the Parametric Catalogue of Italian Earthquakes. Istituto Nazionale
931 di Geofisica e Vulcanologia. doi:http://doi.org/10.6092/INGV.IT-CPTI15, 2016.
932 Scotti, O., Clement, C., and Baumont, D.: Seismic hazard for design and verification
933 of nuclear installations in France: regulatory context, debated issues and
934 ongoing developments, B Geofis Teor Appl, 55, 135-148, 2014.
935 Stein, R. S., King, G. C. P., and Lin, J.: Stress Triggering of the 1994 M=6.7
936 Northridge, California, Earthquake by Its Predecessors, Science, 265, 1432-
937 1435, 1994.
938 Stirling, M., McVerry, G., Gerstenberger, M., Litchfield, N., Van Dissen, R.,
939 Berryman, K., Barnes, P., Wallace, L., Villamor, P., Langridge, R., Lamarche,
940 G., Nodder, S., Reyners, M., Bradley, B., Rhoades, D., Smith, W., Nicol, A.,
941 Pettinga, J., Clark, K., and Jacobs, K.: National Seismic Hazard Model for
942 New Zealand: 2010 Update, B Seismol Soc Am, 102, 1514-1542, 2012.
943 Stock, C. and Smith, E. G. C.: Adaptive kernel estimation and continuous probability
944 representation of historical earthquake catalogs, B Seismol Soc Am, 92, 904-
945 912, 2002a.
946 Stock, C. and Smith, E. G. C.: Comparison of seismicity models generated by
947 different kernel estimations, B Seismol Soc Am, 92, 913-922, 2002b.
948 Stucchi, M., Meletti, C., Montaldo, V., Crowley, H., Calvi, G. M., and Boschi, E.:
949 Seismic Hazard Assessment (2003-2009) for the Italian Building Code, B
950 Seismol Soc Am, 101, 1885-1911, 2011.
951 Verdecchia, A. and Carena, S.: Coulomb stress evolution in a diffuse plate boundary:
952 1400 years of earthquakes in eastern California and western Nevada, USA,
953 Tectonics, 35, 1793-1811, 2016.

954 Visini, F. and Pace, B.: Insights on a Key Parameter of Earthquake Forecasting, the
955 Coefficient of Variation of the Recurrence Time, Using a Simple Earthquake
956 Simulator, Seismol Res Lett, 85, 703-713, 2014.
957 Weichert, D. H: Estimation of the earthquake recurrence parameters for unequal
958 observation periods for different magnitudes, Bulletin of the Seismological
959 Society of America, 70, 1337-1346, 1980.
960 Wells, D. L. and Coppersmith, K. J.: New Empirical Relationships among Magnitude,
961 Rupture Length, Rupture Width, Rupture Area, and Surface Displacement, B
962 Seismol Soc Am, 84, 974-1002, 1994.
963 Werner, M. J., Helmstetter, A., Jackson, D. D., Kagan, Y. Y., and Wiemer, S.:
964 Adaptively smoothed seismicity earthquake forecasts for Italy, Ann Geophys-
965 Italy, 53, 107-116, 2010.
966 Woessner, J., Laurentiu, D., Giardini, D., Crowley, H., Cotton, F., Grunthal, G.,
967 Valensise, G., Arvidsson, R., Basili, R., Demircioglu, M. B., Hiemer, S.,
968 Meletti, C., Musson, R. W., Rovida, A. N., Sesetyan, K., Stucchi, M., and
969 Consortium, S.: The 2013 European Seismic Hazard Model: key components
970 and results, B Earthq Eng, 13, 3553-3596, 2015.
971 Youngs, R. R. and Coppersmith, K. J.: Implications of Fault Slip Rates and
972 Earthquake Recurrence Models to Probabilistic Seismic Hazard Estimates, B
973 Seismol Soc Am, 75, 939-964, 1985.
974 Zechar, J. D. and Jordan, T. H.: Simple smoothed seismicity earthquake forecasts
975 for Italy, Ann Geophys-Italy, 53, 99-105, 2010.
976 Zhao, J. X., Zhang, J., Asano, A., Ohno, Y., Oouchi, T., Takahashi, T., Ogawa, H.,
977 Irikura, K., Thio, H. K., Somerville, P. G., Fukushima, Y., and Fukushima, Y.:
978 Attenuation relations of strong ground motion in Japan using site classification
979 based on predominant period, B Seismol Soc Am, 96, 898-913, 2006.
980

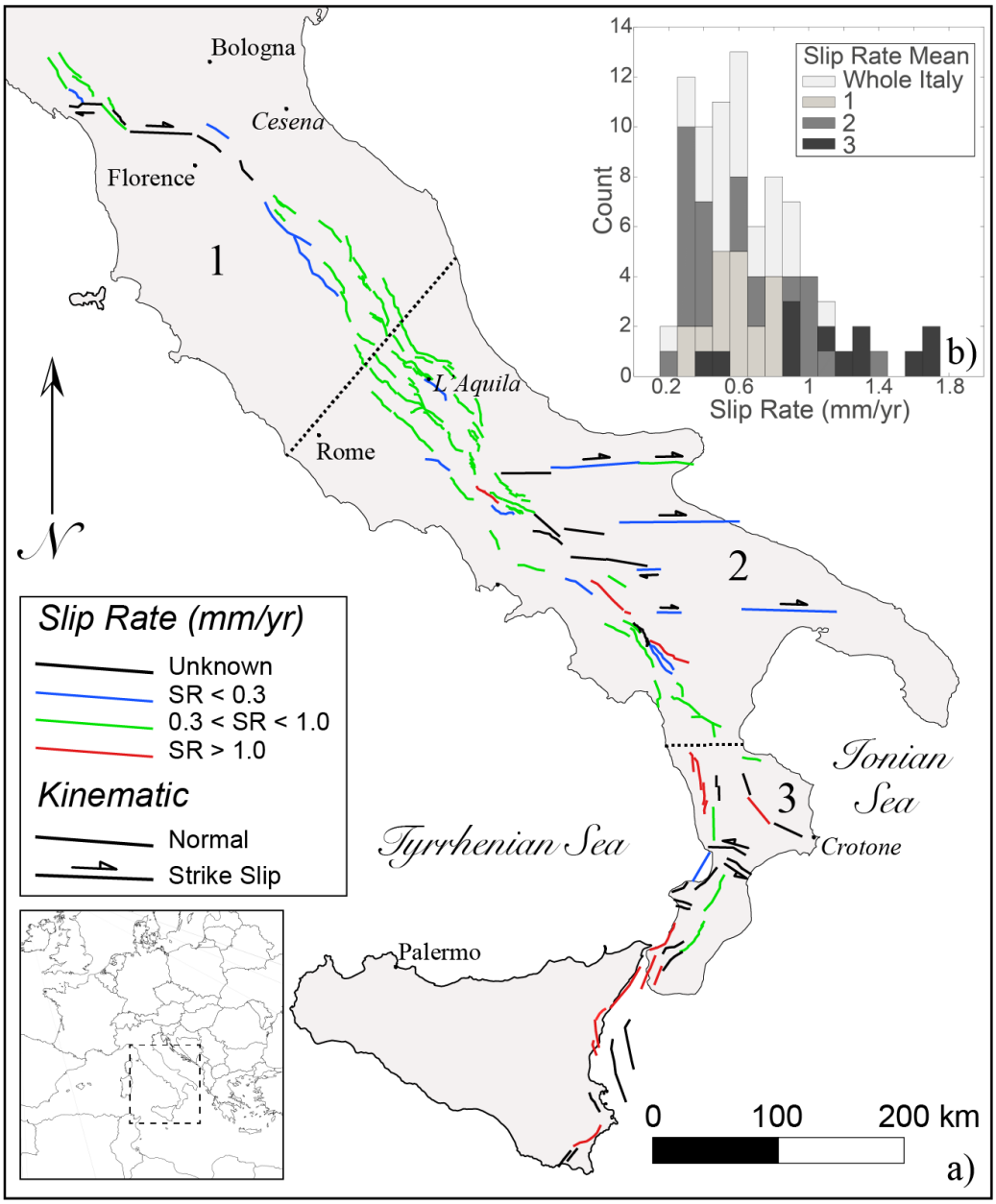

981

982 Fig. 1 a) Map of normal and strike-slip active faults used in this study. The colour
983 scale indicates the slip rate. b) Histogram of the slip rate distribution in the entire
984 study area and in three subsectors. The numbers 1, 2 and 3 represent the Northern
985 Apennines, Central-Southern Apennines and Calabria-Sicilian coast regions,
986 respectively. The dotted black lines are the boundaries of the regions.

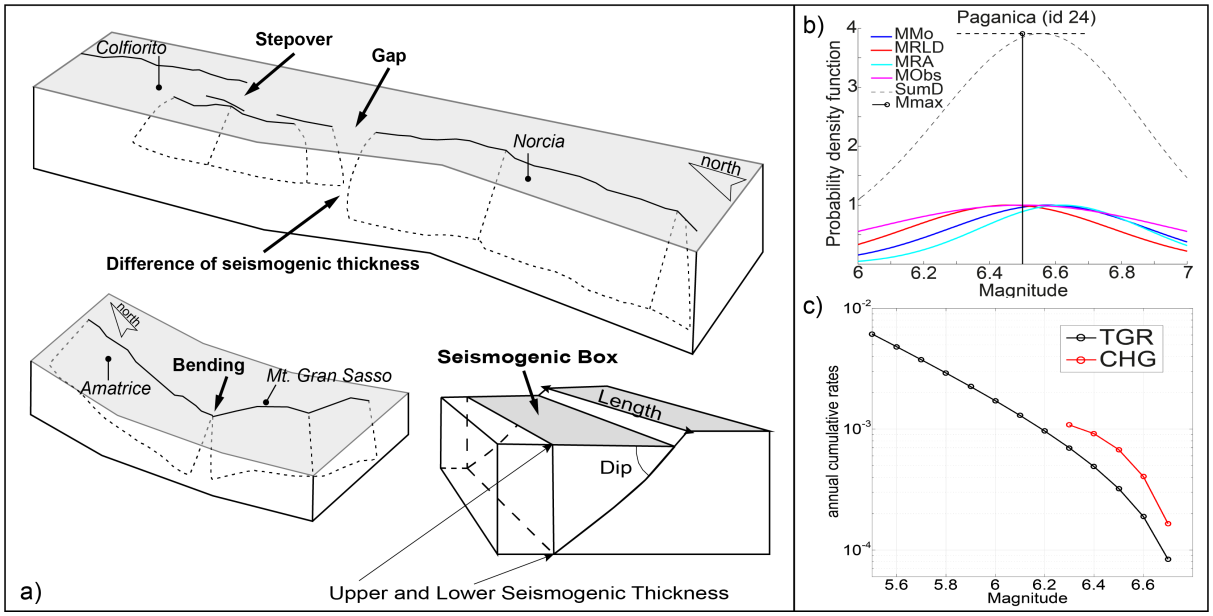

Fig. 2 a) Conceptual model of active faults and segmentation rules adopted to define a fault source and its planar projection, forming a seismogenic box [modified from Boncio et al., 2004]. b) Example of FiSH code output (see Pace et al., 2016 for details) for the Paganica fault source showing the magnitude estimates from empirical relationships and observations, both of which are affected by uncertainties. In this example, four magnitudes are estimated: MMo (blue line) is from the standard formula (IASPEI, 2005); MRLD (red line) and MRA (cyan line) correspond to estimates based on the maximum subsurface fault length and maximum rupture area from the empirical relationships of Wells and Coppersmith (1994) for length and area, respectively; and Mobs (magenta line) is the largest observed moment magnitude. The black dashed line represents the summed probability density curve (SumD), the vertical black line represents the central value of the Gaussian fit of the summed probability density curve (Mmax), and the horizontal black dashed line represents its standard deviation (σMmax). The input values that were used to obtain this output are provided in Table 1. c) Comparison of the magnitude–frequency distributions of the Paganica source, which were obtained using the CHG model (red line) and the TGR model (black line).

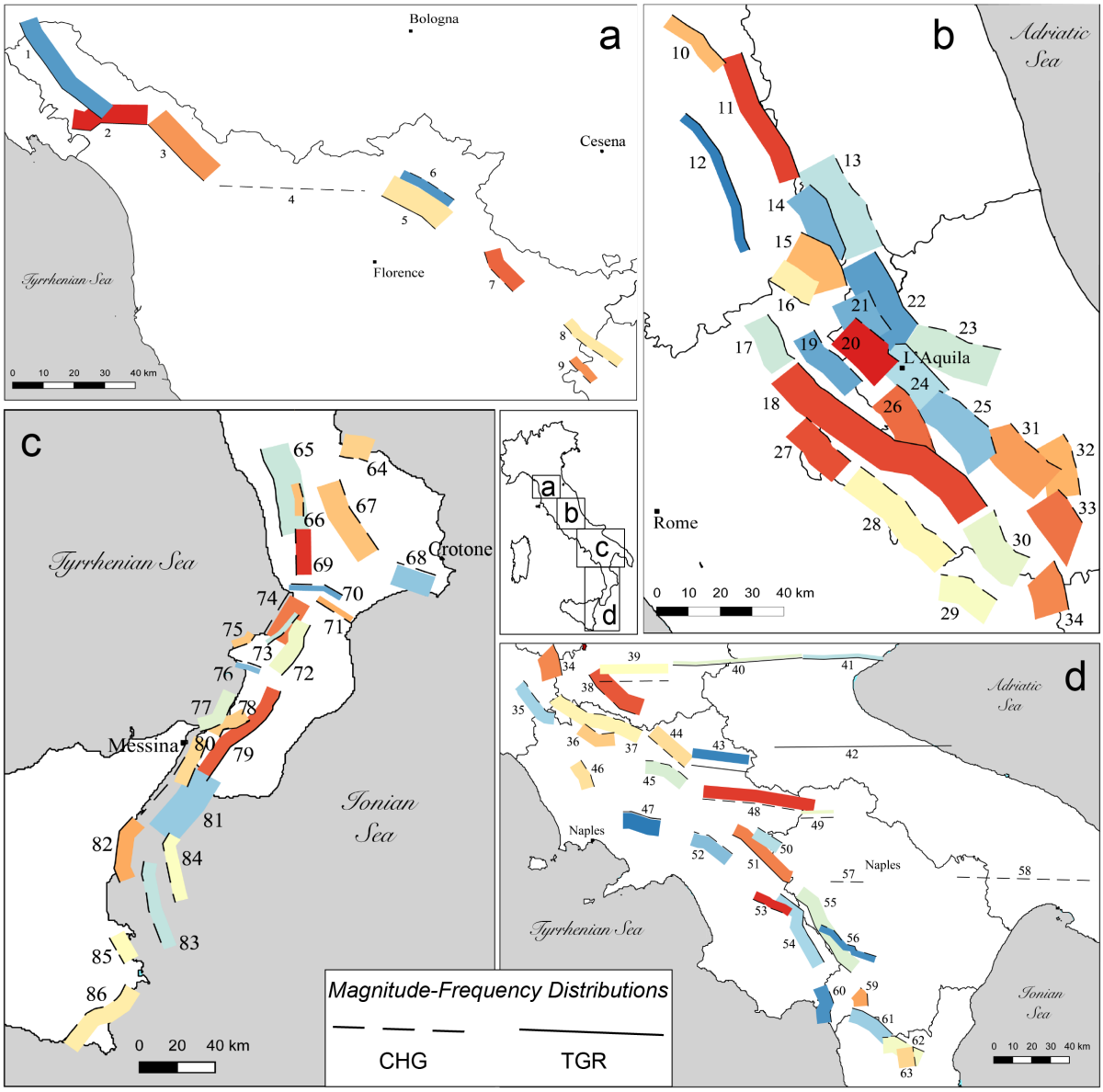

Fig. 3 Maps showing the fault source inputs as seismogenic boxes (see Fig. 2a). The colour scale indicates the activity rate. Solid and dashed lines (corresponding to the uppermost edge of the fault) are used to highlight our choice between the two end-members of the MFD model adopted in the so-called *Mixed* model.

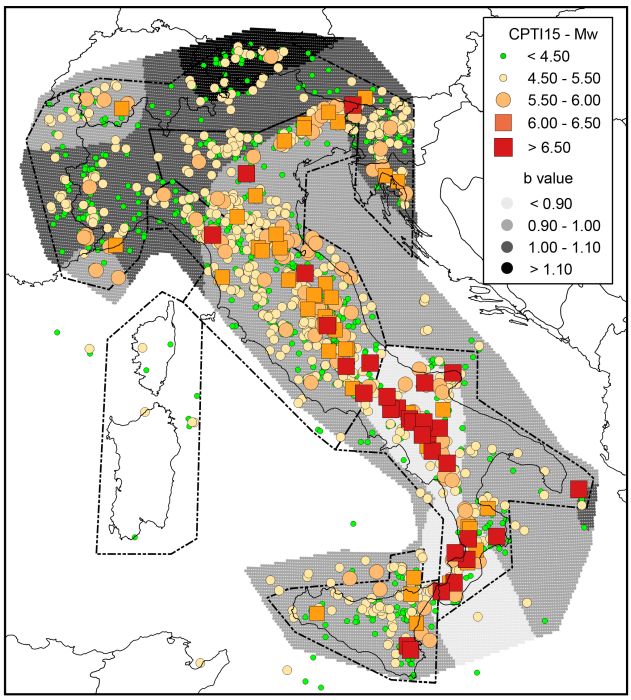

Fig. 4 Historical earthquakes from the most recent version of the historical parametric Italian catalogue (CPTI15, Rovida et al., 2016), the spatial variations in b-values and the polygons defining the five macroseismic areas used to assess the magnitude intervals.

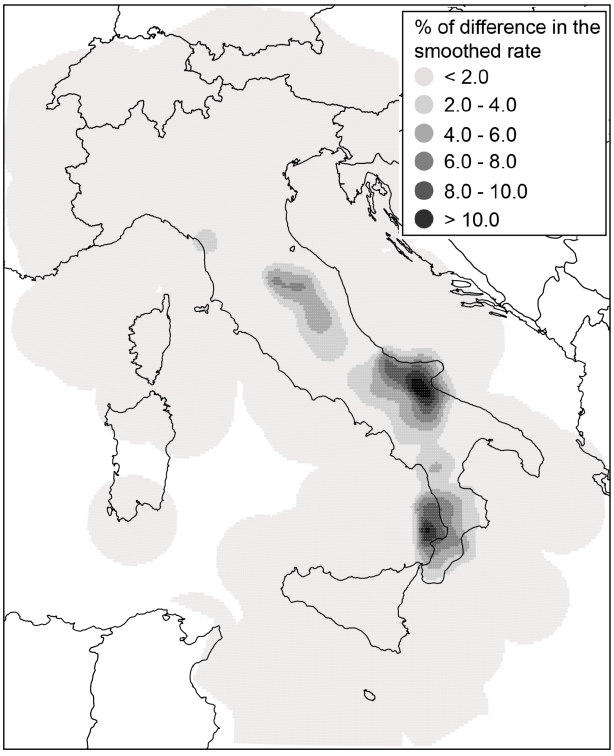

Fig. 5 Differences in percentages between the two smoothed rates produced by eq. (2) using the complete catalogue and the modified catalogue without events associated with known active faults (*TGR* model)

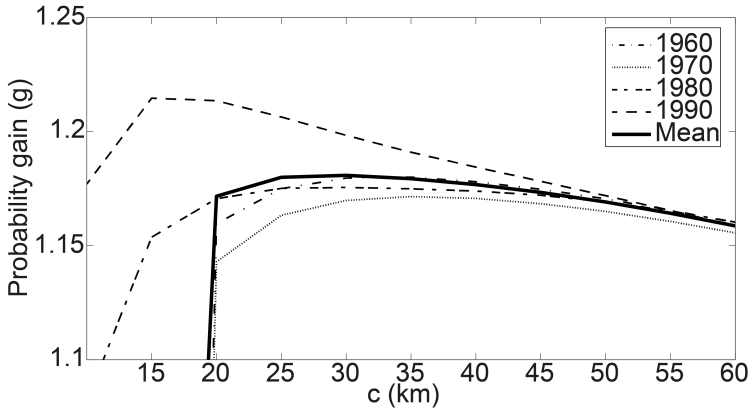

Fig. 6 Probability gain per earthquake (see eq. 3) versus correlation distance *c*, highlighting the best radius for use in the smoothed seismicity approach (eq. 2)

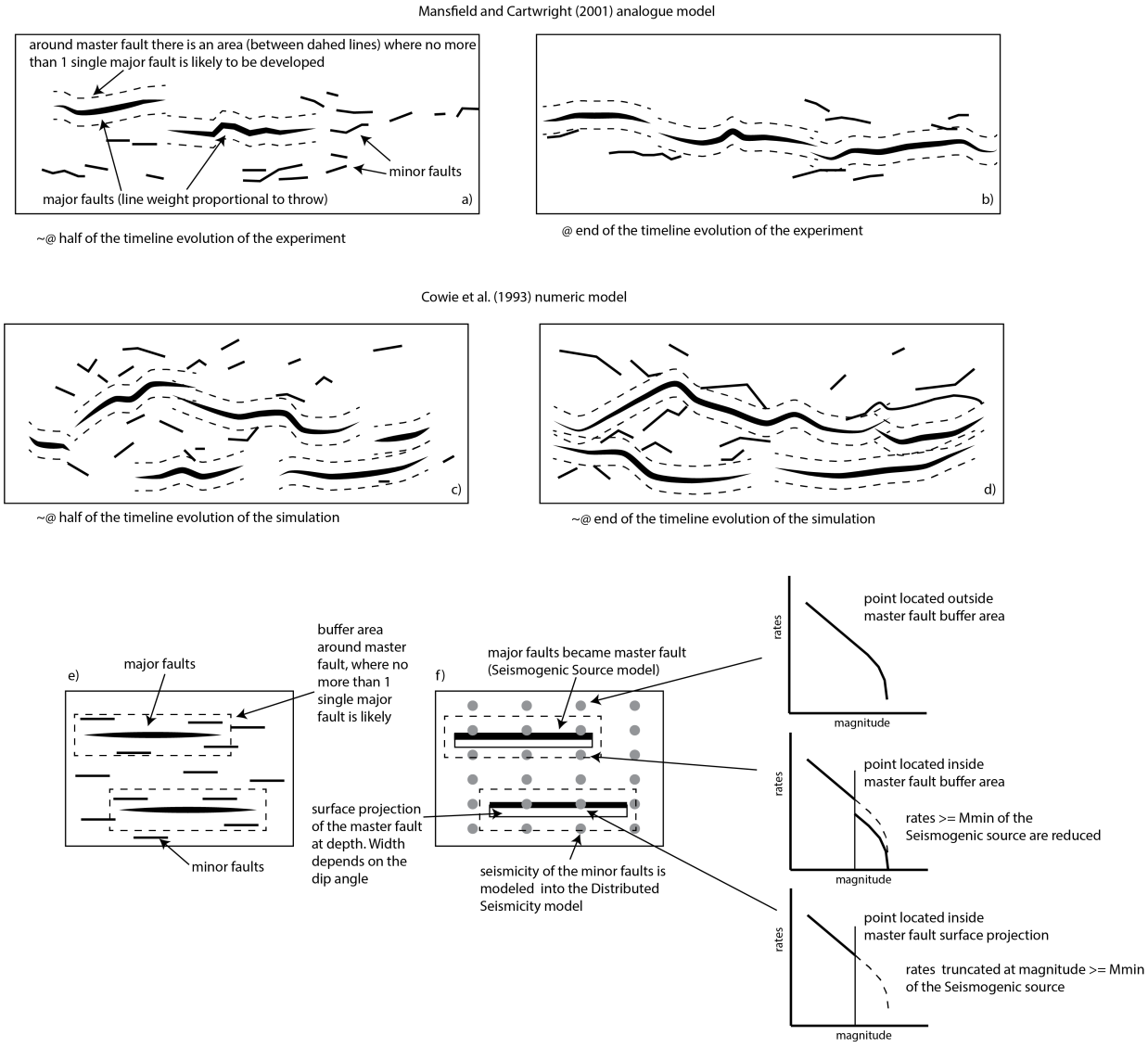

Fig. 7 Fault system evolution and implications in our model. a) and b) Diagrams from the Mansfield and Cartwright (2001) analogue experiment in two different stages: the approximate midpoint of the sequence and the end of the sequence. Areas exist around master faults where no more than a single major fault is likely to develop. c) and d) Diagrams from numerical modelling conducted by Cowie et al. (1993) in two different stages. This experiment shows the similar evolutional features of major and minor faults. e) and f) Application of the analogue and numerical modelling of fault system evolution to the fault source input proposed in this paper. A buffer area is drawn around each fault source, where it is unlikely for other major faults to develop, and it accounts for the length and slip rate of the fault source. This buffer area is useful for reducing or truncating the rates of expected distributed seismicity based on the position of a distributed seismicity point with respect to the buffer zone (see the text for details).

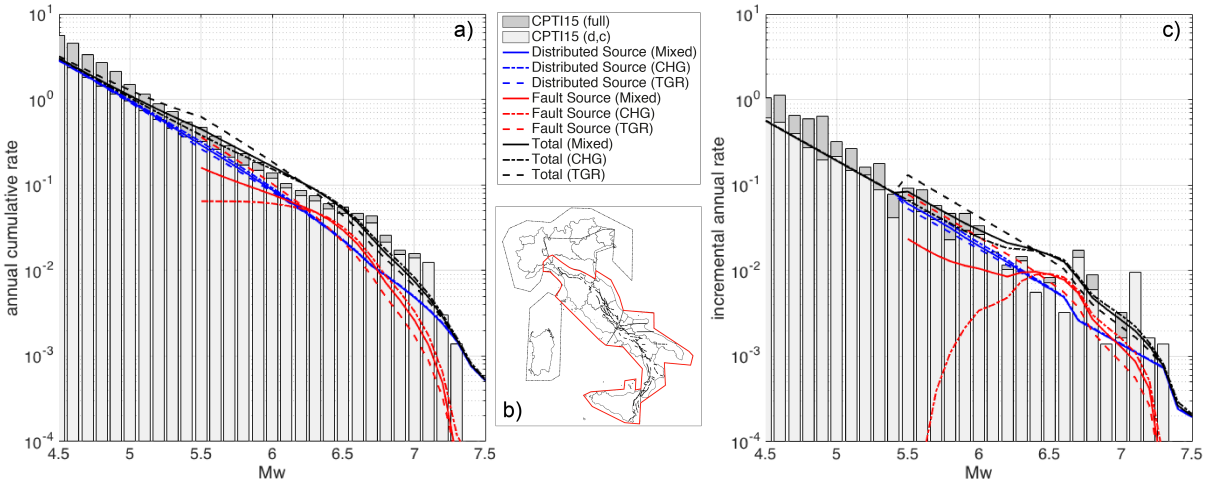

Fig. 8 a) annual cumulative rate and c) incremental annual rate computed for the red bounded area in b). The rates have been computed using: (i) the full CPTI15 catalogue; (ii) the declustered and complete catalogue (CPTI15 (d, c) in the legend) obtained using the completeness magnitude thresholds over different periods of time given by Stucchi et al. (2011) for five large zones; (iii) the distributed sources; (iv) the fault sources; and (v) summing fault and distributed sources (Total).

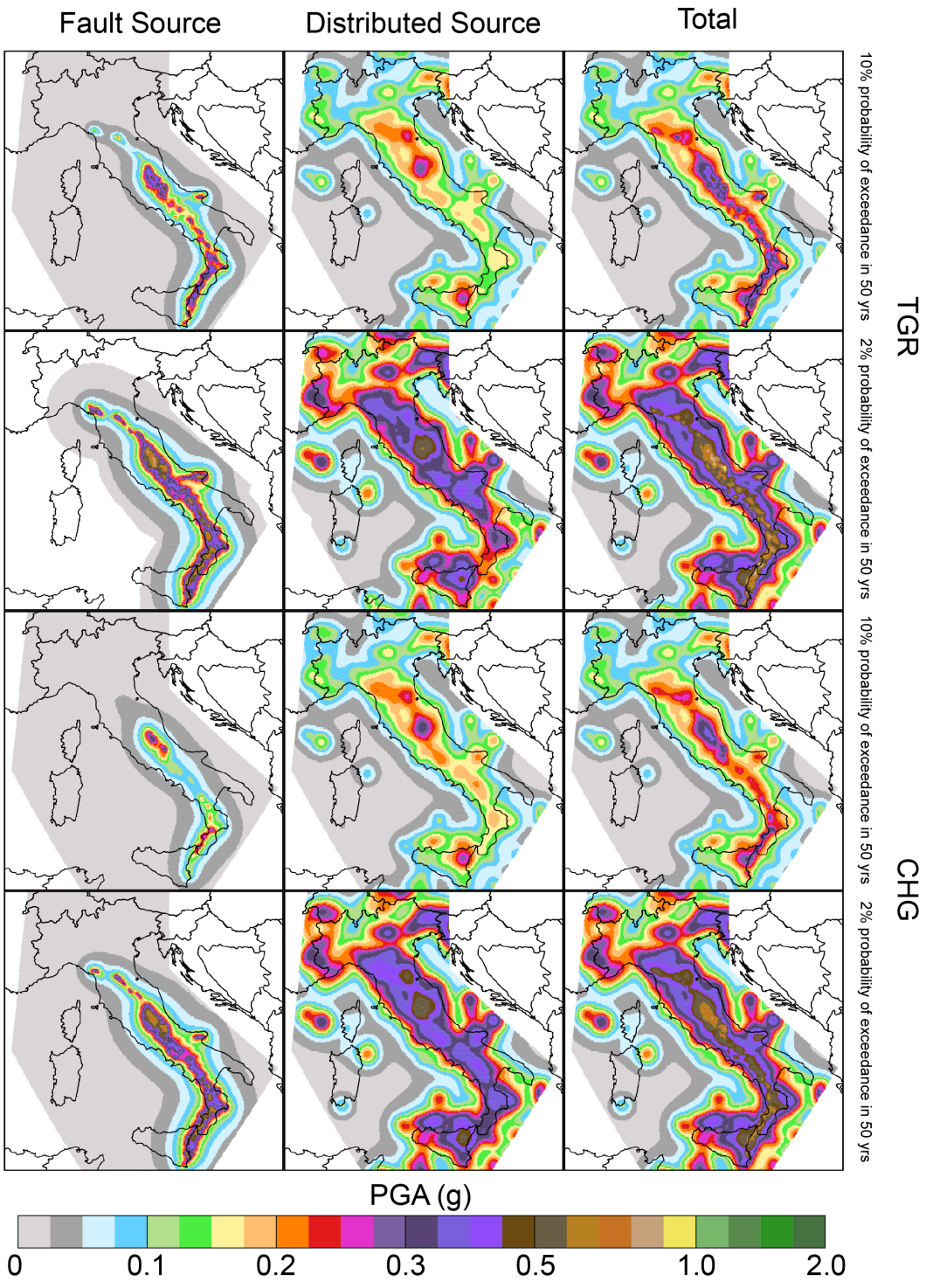

Fig. 9 Seismic hazard maps for the *TGR* and *CHG* models expressed in terms of peak ground acceleration (PGA) and computed for a latitude/longitude grid spacing of 0.05°. The first and second rows show the fault source, distributed source and total maps of the *TGR* model computed for 10% probability of exceedance in 50 years and 2% probability of exceedance in 50 years, corresponding to return periods of 475 and 2475 years, respectively. The third and fourth rows show the same maps for the *CHG* model.

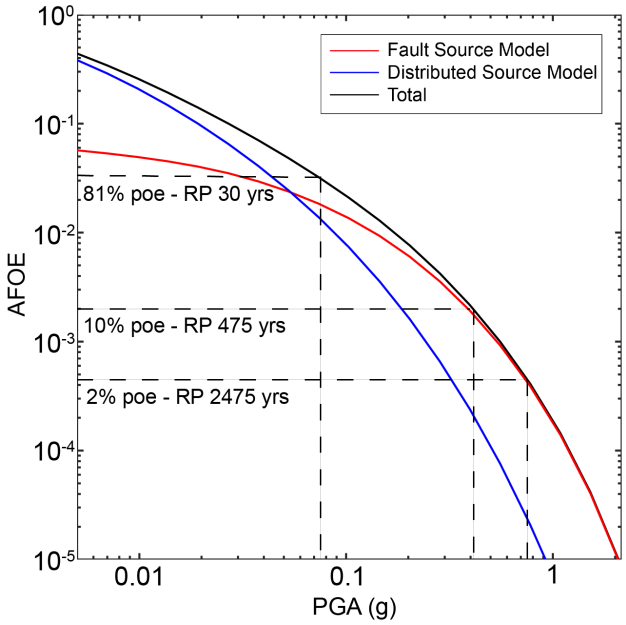

Fig. 10 An example of the contribution to the total seismic hazard level (black line), in terms of hazard curves, by the *fault* (red line) and *distributed* (blue line) source inputs for one of the 45,602 grid points (L'Aquila, 42.400-13.400). The dashed lines represent the 2%, 10% and 81% probabilities of exceedance (poes) in 50 years.

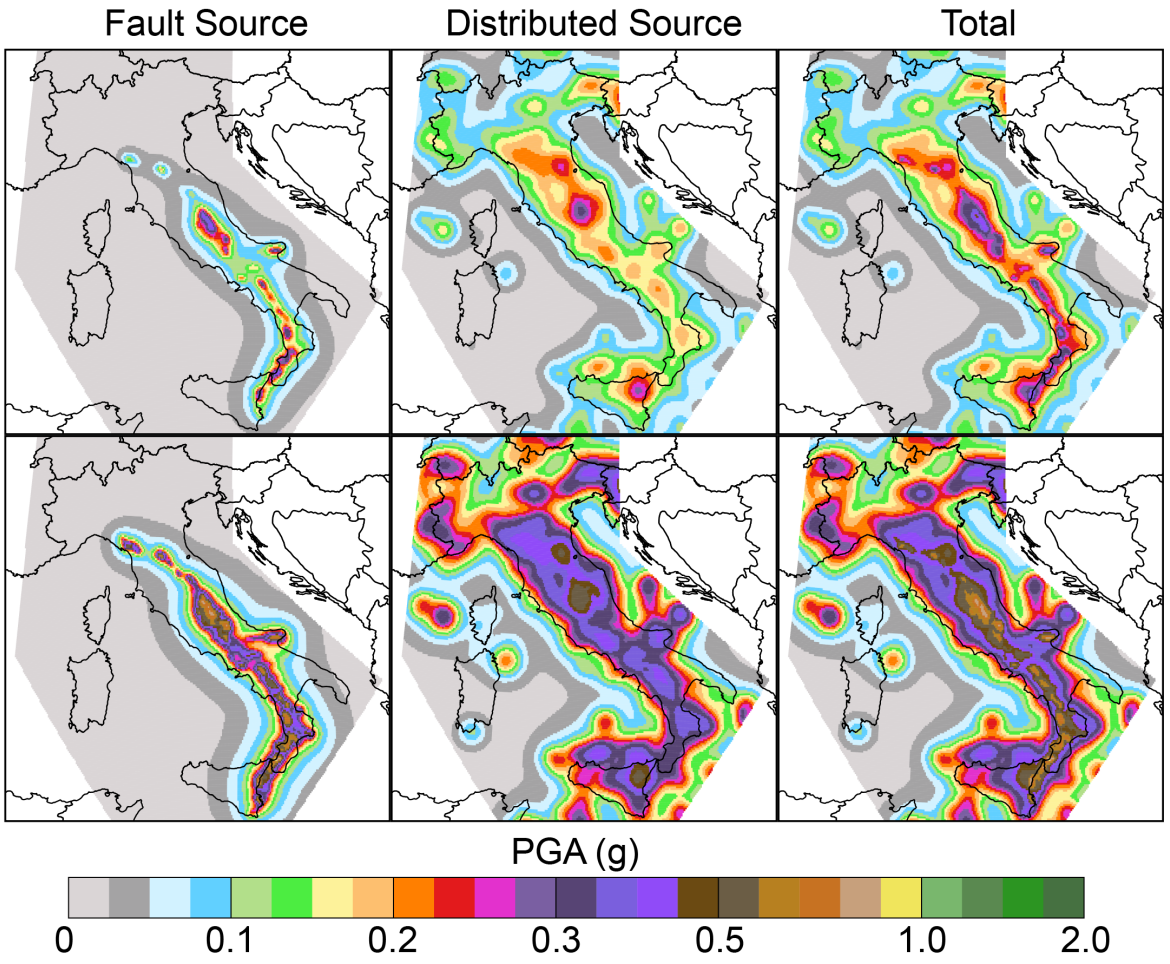

Fig. 11 Seismic hazard maps for the *Mixed* model. The first row shows the fault source, distributed source and total maps computed for 10% probability of exceedance in 50 years, and the second row shows the same maps but computed for 2% probability of exceedance in 50 years, corresponding to return periods of 475 and 2475 years, respectively. The results are expressed in terms of peak ground acceleration (PGA).

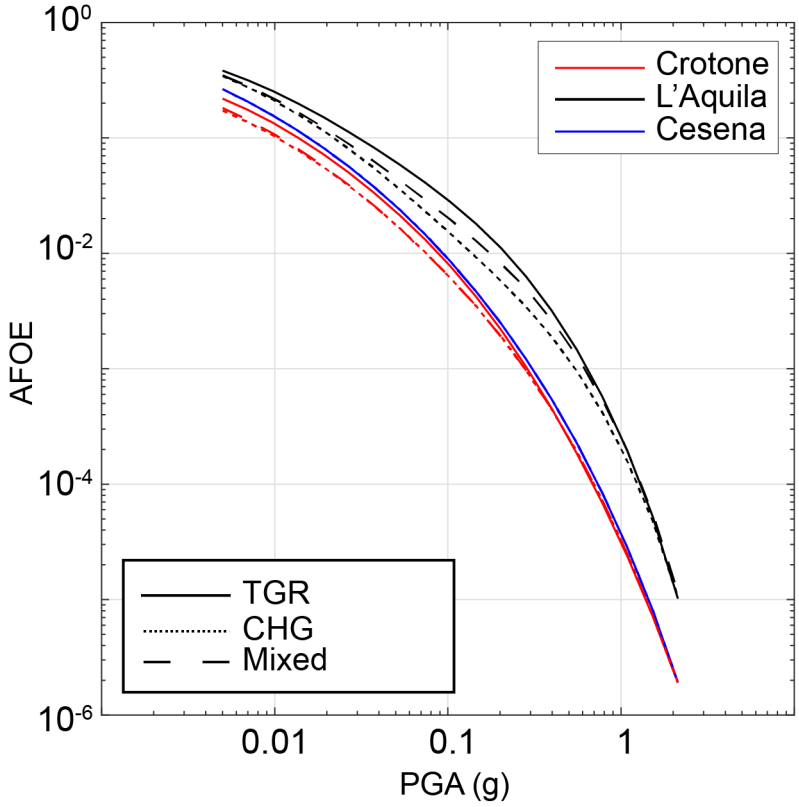

Fig. 12 *CHG* (dotted line), *TGR* (solid line) and *Mixed* model (dashed line) hazard curves for three sites: Cesena (red line), L'Aquila (black line) and Crotone (blue line)

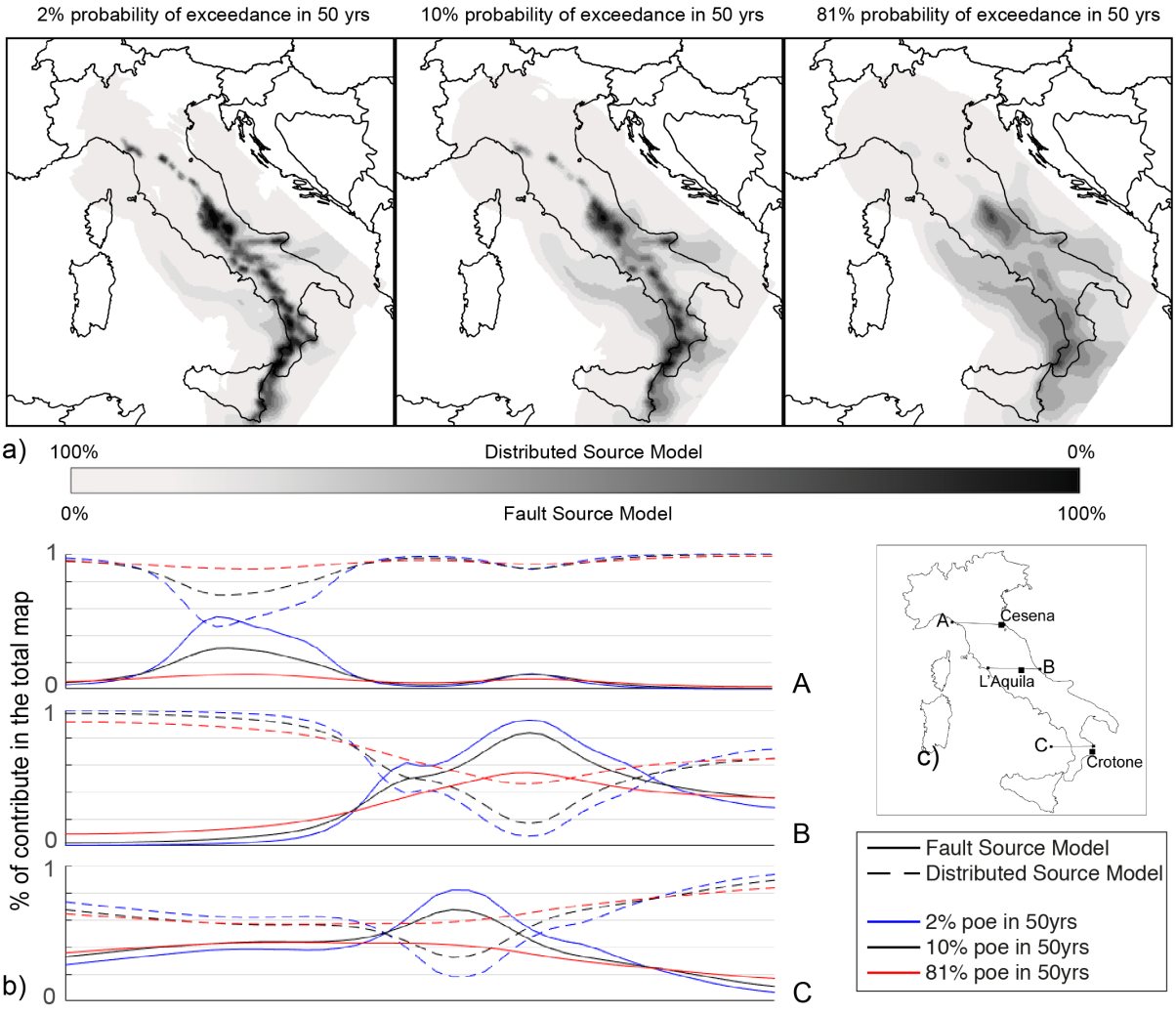

Fig. 13 a) Contribution maps of the Mixed *fault* and *distributed* source inputs to the total hazard level for three probabilities of exceedance: 2%, 10% and 81%, corresponding to return periods of 2475, 475 and 30 years, respectively. b) Contributions of the Mixed *fault* (solid line) and *distributed* (dashed line) source inputs along three profiles (A, B and C in Fig. 13c) for three probabilities of exceedance: 2% (blue line), 10% (black line) and 81% (red line).

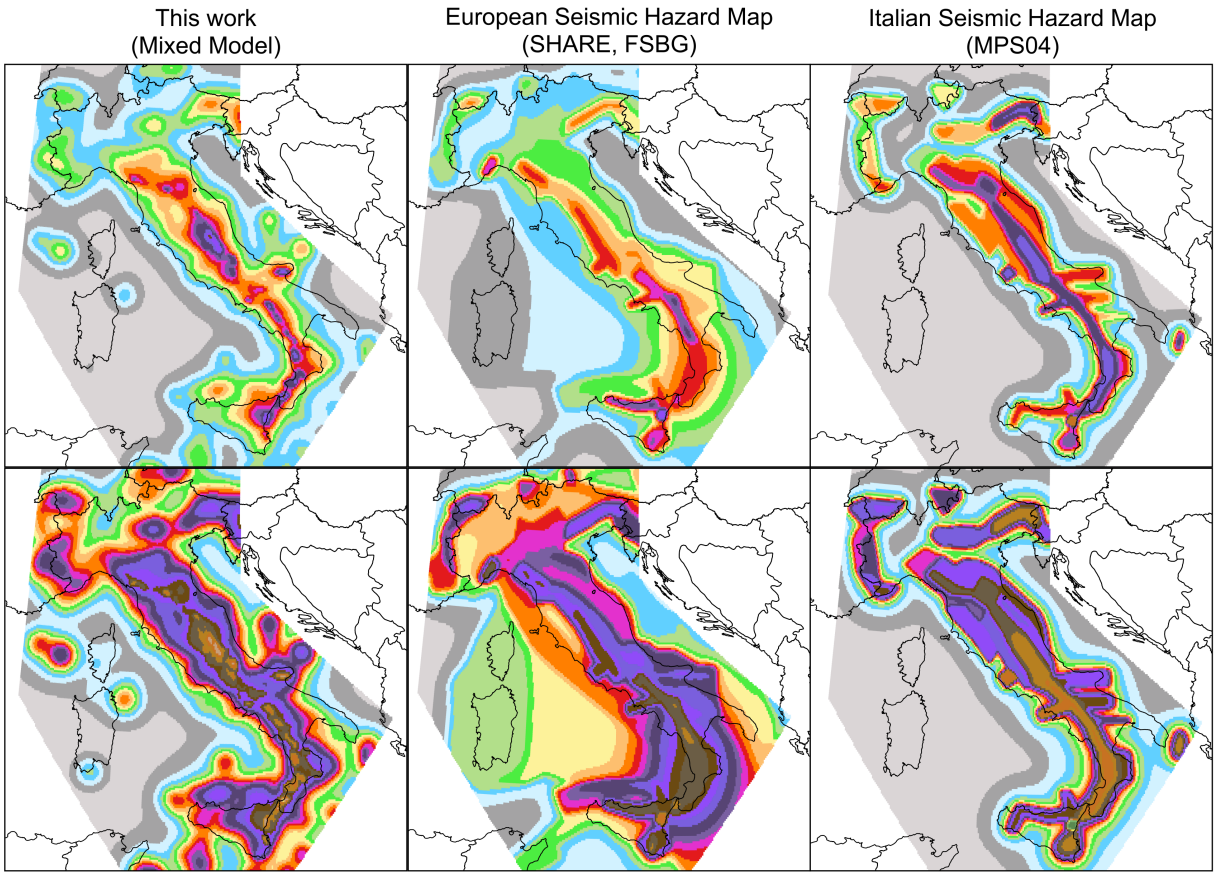

Fig. 14 Seismic hazard maps expressed in terms of Peak Ground Acceleration (PGA) and computed for a latitude/longitude grid spacing of 0.05° based on site conditions. The figure shows a comparison of our model (*Mixed* model, on the left), the SHARE model (FSBG logic tree branch, in the middle) and the current Italian national seismic hazard map (MPS04, on the right). The same GMPEs (Akkar et al. 2013, Chiou et al., 2008, Faccioli et al., 2010 and Zhao et al., 2006 and Bindi et al. 2014), were used for all models to obtain and compare the maps.

ID	Fault Sources	L (km)	Dip (°)	Upper (km)	Lower (km)	SR_{min} (mm/yr)	SR_{max} (mm/yr)
1	Lunigiana	43.8	40	0	5	0.28	0.7
2	North Apuane Transfer	25.5	45	0	7	0.33	0.83
3	Garfagnana	26.9	30	0	4.5	0.35	0.57
4	Garfagnana Transfer	47.1	90	2	7	0.33	0.83
5	Mugello	21.0	40	0	7	0.33	0.83
6	Ronta	19.3	65	0	7	0.17	0.5
7	Poppi	17.1	40	0	4.5	0.33	0.83
8	Città di Castello	22.9	40	0	3	0.25	1.2
9	M.S.M. Tiberina	10.5	40	0	2.5	0.25	0.75
10	Gubbio	23.6	50	0	6	0.4	1.2
11	Colfiorito System	45.9	50	0	8	0.25	0.9
12	Umbra Valley	51.1	55	0	4.5	0.4	1.2
13	Vettore-Bove	35.4	50	0	15	0.2	1.05
14	Nottoria-Preci	29.0	50	0	12	0.2	1
15	Cascia-Cittareale	24.3	50	0	13.5	0.2	1
16	Leonessa	14.9	55	0	12	0.1	0.7
17	Rieti	17.6	50	0	10	0.25	0.6
18	Fucino	82.3	50	0	13	0.3	1.6
19	Sella di Corno	23.1	60	0	13	0.35	0.7
20	Pizzoli-Pettino	21.3	50	0	14	0.3	1
21	Montereale	15.1	50	0	14	0.25	0.9
22	Gorzano	28.1	50	0	15	0.2	1
23	Gran Sasso	28.4	50	0	15	0.35	1.2
24	Paganica	23.7	50	0	14	0.4	0.9
25	Middle Aternum Valley	29.1	50	0	14	0.15	0.45
26	Campo Felice-Ovindoli	26.2	50	0	13	0.2	1.6
27	Carsoli	20.5	50	0	11	0.35	0.6
28	Liri	42.5	50	0	11	0.3	1.26
29	Sora	20.4	50	0	11	0.15	0.45
30	Marsicano	20.0	50	0	13	0.25	1.2
31	Sulmona	22.6	50	0	15	0.6	1.35
32	Maiella	21.4	55	0	15	0.7	1.6
33	Aremogna C.Miglia	13.1	50	0	15	0.1	0.6
34	Barrea	17.1	55	0	13	0.2	1
35	Cassino	24.6	60	0	11	0.25	0.5
36	Ailano-Piedimonte	17.6	60	0	12	0.15	0.35
37	Matese	48.3	60	0	13	0.2	1.9
38	Bojano	35.5	55	0	13	0.2	0.9
39	Frosolone	36.1	70	11	25	0.35	0.93
40	Ripabottoni-San Severo	68.3	85	6	25	0.1	0.5
41	Mattinata	42.3	85	0	25	0.7	1
42	Castelluccio dei Sauri	93.2	90	11	22	0.1	0.5
43	Ariano Irpino	30.1	70	11	25	0.35	0.93
44	Tammaro	25.0	60	0	13	0.35	0.93
45	Benevento	25.0	55	0	10	0.35	0.93
46	Volturno	15.7	60	1	13	0.23	0.57
47	Avella	20.5	55	1	13	0.2	0.7
48	Ufita-Bisaccia	59.0	64	1.5	15	0.35	0.93
49	Melfi	17.2	80	12	22	0.1	0.5
50	Irpinia Antithetic	15.0	60	0	11	0.2	0.53

51	Irpinia	39.7	65	0	14	0.3	2.5
52	Volturara	23.7	60	1	13	0.2	0.35
53	Alburni	20.4	60	0	8	0.35	0.7
54	Caggiano-Diano Valley	46.0	60	0	12	0.35	1.15
55	Pergola-Maddalena	50.6	60	0	12	0.20	0.93
56	Agri	34.9	50	5	15	0.8	1.3
57	Potenza	17.8	90	15	21	0.1	0.5
58	Palagianello	73.3	90	13	22	0.1	0.5
59	Monte Alpi	10.9	60	0	13	0.35	0.9
60	Maratea	21.6	60	0	13	0.46	0.7
61	Mercure	25.8	60	0	13	0.2	0.6
62	Pollino	23.8	60	0	15	0.22	0.58
63	Castrovillari	10.3	60	0	15	0.2	1.15
64	Rossano	14.9	60	0	22	0.5	0.6
65	Crati West	49.7	45	0	15	0.84	1.4
66	Crati East	18.4	60	0	8	0.75	1.45
67	Lakes	43.6	60	0	22	0.75	1.45
68	Fuscalto	21.1	60	2	22	0.75	1.45
69	Piano Lago-Decollatura	25.0	60	1	15	0.23	0.57
70	Catanzaro North	29.5	80	3	20	0.75	1.45
71	Catanzaro South	21.3	80	3	20	0.75	1.45
72	Serre	31.6	60	0	15	0.7	1.15
73	Vibo	23.0	80	0	15	0.75	1.45
74	Sant'Eufemia Gulf	24.8	40	1	11	0.11	0.3
75	Capo Vaticano	13.7	60	0	8	0.75	1.45
76	Coccorino	13.3	70	3	11	0.75	1.45
77	Scilla	29.7	60	0	13	0.8	1.5
78	Sant'Eufemia	19.2	60	0	13	0.75	1.45
79	Cittanova-Armo	63.8	60	0	13	0.45	1.45
80	Reggio Calabria	27.2	60	0	13	0.7	2
81	Taormina	38.7	30	3	13	0.9	2.6
82	Acireale	39.4	60	0	15	1.15	2.3
83	Western Ionian	50.1	65	0	15	0.75	1.45
84	Eastern Ionian	39.3	65	0	15	0.75	1.45
85	Climiti	15.7	60	0	15	0.75	1.45
86	Avola	46.9	60	0	16	0.8	1.6

Table 1 Geometric Parameters of the Fault Sources. L, along-strike length; Dip, inclination angle of the fault plane; Upper and Lower, the thickness bounds of the local seismogenic layer; SRmin and SRmax, the slip rates assigned to the sources using the references available (see the supplemental files); and *ID,* the fault number identifier.

		Historical Earthquakes					Instrumental Earthquakes	
ID	Fault Sources	yyyy/mm/dd	I_{Max}	I_0	M_w	*sD*	yyyy/mm/dd	M_w
1	Lunigiana	1481/05/07	VIII	VIII	5.6	0.4		
		1834/02/14	IX	IX	6.0	0.1		
2	North Apuane Transfer	1837/04/11	X	IX	5.9	0.1		
3	Garfagnana	1740/03/06	VIII	VIII	5.6	0.2		
		1920/09/07	X	X	6.5	0.1		
4	Garfagnana Transfer							
5	Mugello	1542/06/13	IX	IX	6.0	0.2		
		1919/06/29	X	X	6.4	0.1		
6	Ronta							
7	Poppi							
8	Città di Castello	1269			5.7			
		1389/10/18	IX	IX	6	0.5		
		1458/04/26	VIII-IX	VIII-IX	5.8	0.5		
		1789/09/30	IX	IX	5.9	0.1		
9	M.S.M. Tiberina	1352/12/25	IX	IX	6.3	0.2		
		1917/04/26	IX-X	IX-X	6.0	0.1		
10	Gubbio						1984/04/29	5.6
11	Colfiorito System	1279/04/30	X	IX	6.2	0.2	1997/09/26	5.7
		1747/04/17	IX	IX	6.1	0.1	1997/09/26	6
		1751/07/27	X	X	6.4	0.1		
12	Umbra Valley	1277		VIII	5.6	0.5		
		1832/01/13	X	X	6.4	0.1		
		1854/02/12	VIII	VIII	5.6	0.3		
13	Vettore-Bove						2016/10/30	6.5
14	Nottoria-Preci	1328/12/01	X	X	6.5	0.3	1979/09/19	5.8
		1703/01/14	XI	XI	6.9	0.1		
		1719/06/27	VIII	VIII	5.6	0.3		
		1730/05/12	IX	IX	6.0	0.1		
		1859/08/22	VIII-IX	VIII-IX	5.7	0.3		
		1879/02/23	VIII	VIII	5.6	0.3		
15	Cascia-Cittareale	1599/11/06	IX	IX	6.1	0.2		
		1916/11/16	VIII	VIII	5.5	0.1		
16	Leonessa							
17	Rieti	1298/12/01	X	IX-X	6.3	0.5		
		1785/10/09	VIII-IX	VIII-IX	5.8	0.2		
18	Fucino	1349/09/09	IX	IX	6.3	0.1		
		1904/02/24	IX	VIII-IX	5.7	0.1		
		1915/01/13	XI	XI	7	0.1		
19	Sella di Corno							
20	Pizzoli-Pettino	1703/02/02	X	X	6.7	0.1		
21	Montereale							
22	Gorzano	1639/10/07	X	IX-X	6.2	0.2		
		1646/04/28	IX	IX	5.9	0.4		
23	Gran Sasso							
24	Paganica	1315/12/03	VIII	VIII	5.6	0.5	2009/06/04	6.3
		1461/11/27	X	X	6.5	0.5		
25	Middle Aternum Valley							
26	Campo Felice-Ovindoli							
27	Carsoli							
28	Liri							
29	Sora	1654/07/24	X	IX-X	6.3	0.2		
30	Marsicano							
31	Sulmona							
32	Maiella							
33	Aremogna C.Miglia							
34	Barrea						1984/05/07	5.9
35	Cassino							
36	Ailano-Piedimonte							
37	Matese	1349/09/09	X-XI	X	6.8	0.2		

38	Bojano	1805/07/26	X	X	6.7	0.1		
39	Frosolone	1456/12/05	XI	XI	7	0.1		
40	Ripabottoni-San Severo	1627/07/30	X	X	6.7	0.1	2002/10/31	5.7
		1647/05/05	VII-VIII	VII-VIII	5.7	0.4		
		1657/01/29	IX-X	VIII-IX	6.0	0.2		
41	Mattinata	1875/12/06	VIII	VIII	5.9	0.1		
		1889/12/08	VII	VII	5.5	0.1		
		1948/08/18	VII-VIII	VII-VIII	5.6	0.1		
42	Castelluccio dei Sauri	1361/07/17	X	IX	6	0.5		
		1560/05/11	VIII	VIII	5.7	0.5		
		1731/03/20	IX	IX	6.3	0.1		
43	Ariano Irpino	1456/12/05			6.9	0.1		
		1962/08/21	IX	IX	6.2	0.1		
44	Tammaro	1688/06/05	XI	XI	7	0.1		
45	Benevento							
46	Volturno							
47	Avella	1499/12/05	VIII	VIII	5.6	0.5		
48	Ufita-Bisaccia	1732/11/29	X-XI	X-XI	6.8	0.1		
		1930/07/23	X	X	6.7	0.1		
49	Melfi	1851/08/14	X	X	6.5	0.1		
50	Irpinia Antithetic							
51	Irpinia	1466/01/15	VIII-IX	VIII-IX	6.0	0.2	1980/11/23	6.8
		1692/03/04	VIII	VIII	5.9	0.4		
		1694/09/08	X	X	6.7	0.1		
		1853/04/09	IX	VIII	5.6	0.2		
52	Volturara							
53	Alburni							
54	Caggiano-Diano Valley	1561/07/31	IX-X	X	6.3	0.1		
55	Pergola-Maddalena	1857/12/16			6.5			
		1857/12/16			6.3			
56	Agri							
57	Potenza	1273/12/18	VIII-IX	VIII-IX	5.8	0.5	1990/05/05	5.8
58	Palagianello							
59	Monte Alpi							
60	Maratea							
61	Mercure	1708/01/26	VIII-IX	VIII	5.6	0.6	1998/09/09	5.5
62	Pollino							
63	Castrovillari							
64	Rossano	1836/04/25	X	IX	6.2	0.2		

65	Crati West	1184/05/24	IX	IX	6.8	0.3
		1870/10/04	X	IX-X	6.2	0.1
		1886/03/06	VII-VIII	VII-VIII	5.6	0.3
66	Crati East	1767/07/14	VIII-IX	VIII-IX	5.9	0.2
		1835/10/12	X	IX	5.9	0.3
67	Lakes	1638/06/08	X	X	6.8	0.1
68	Fuscalto	1832/03/08	X	X	6.6	0.1
69	Piano Lago-Decollatura					
70	Catanzaro North	1638/03/27			6.6	
71	Catanzaro South	1626/04/04	X	IX	6.1	0.4
72	Serre	1659/11/05	X	X	6.6	0.1
		1743/12/07	IX-X	VIII-IX	5.9	0.2
		1783/02/07	X-XI	X-XI	6.7	0.1
		1791/10/13	IX	IX	6.1	0.1
73	Vibo					
74	Sant'Eufemia Gulf	1905/09/08	X-XI	X-XI	7	0.1
75	Capo Vaticano					
76	Coccorino	1928/03/07	VIII	VII-VIII	5.9	0.1
77	Scilla					
78	Sant'Eufemia	1894/11/16	IX	IX	6.1	0.1
79	Cittanova-Armo	1509/02/25	IX	VIII	5.6	0.4
		1783/02/05	XI	XI	7.1	0.1
80	Reggio Calabria					
81	Taormina	1908/12/28	XI	XI	7.1	0.2
82	Acireale	1818/02/20	IX-X	IX-X	6.3	0.1
83	Western Ionian	1693/01/11	XI	XI	7.3	0.1
84	Eastern Ionian					
85	Climiti					
86	Avola					

1103

1104 Table 2 Earthquake-Source Association Adopted for Fault Sources. $I_{Max,}$ maximum
1105 intensity; I_0, epicentral intensity; M_w, moment magnitude; and sD, standard deviation
1106 of the moment magnitude. For references, see the supplemental files.